

Lund University

MASTER THESIS

Development of a Detector
System for Detection of
Thermal Neutrons from
Spent Nuclear Fuel

Author: Daniel Söderström

Supervisor: Dr. Linus Ros

Co-supervisor: Prof. Per Kristiansson



LUND
UNIVERSITY

2016-06-09

Abstract

The nuclear reaction $^{10}\text{B}(n, \alpha)^7\text{Li}^*$ was utilised to develop a neutron detection system. This system has the purpose of being used to detect the thermal neutron radiation emitted by spent nuclear fuel, before it is transported to a final repository. This to investigate the content of the fuel-containing capsules, primarily to ensure non-proliferation of radioactive materials in the nuclear waste management process.

The investigated detector system utilises two scintillators mounted on one photomultiplier tube (PMT). One of them boron loaded to be sensitive to neutrons, and the other sensitive to gamma radiation to detect the de-excitation quanta released by the lithium ion, often left in an excited state after the $^{10}\text{B}(n, \alpha)^7\text{Li}^*$ reaction. The detection of these signals together reduces background noise, and those signals of interest are extracted from the others by a pulse shape discrimination scheme.

The possibility to read out the scintillator signals using an avalanche photodiode (APD) was also investigated. Inherent noise difficulties and poorly matched properties of scintillators and APDs made read out with APDs difficult.

Studies of boron carbide (B_4C) coated plastic scintillators and diodes were conducted as well. A neutron detection method using boron carbide coated diodes was tested. Proof of concept measurements were made using such coated diodes. The effect on the properties of plastic scintillators when coated with B_4C were qualitatively assessed.

Preface

This thesis is a part of a collaboration project between The Swedish Nuclear Fuel and Waste Management Company (SKB) and the Lund Ion Beam Analysis Facility (LIBAF) group at the nuclear physics department in the institution of physics of Lund University. The measurements and the experiments presented have been conducted at the micro beam laboratory at the institution of physics of Lund University during the spring of 2016.

The whole division of nuclear physics, and the LIBAF group in particular, has provided a very welcoming and helpful environment both in a professional and personal sense. Everybody at the workplace, not only the permanent employees, has been welcomed to join in both administrative meetings as well as on activities and excursions which created a feeling of inclusion that I did not expect beforehand. Thank you all.

I want to especially thank my supervisor Linus Ros and my co-supervisor Per Kristiansson for everlasting support and aid, and for finding time to assist me even though my supervisor had his own disputation to attend to.

Thank you Mikael Elfman for sharing the DAQ system, and for sharing so much valuable information regarding physics experiments.

Anton Roth deserves special recognition as well, for sitting by my side and providing good company through the duration of this project. Also for being a good sounding board for ideas, and for being there to discuss physical concepts (and occasionally other topics as well).

Populärvetenskaplig sammanfattning

I Sverige har en stor del av den elektricitet vi använder i vardagen kommit från kärnkraftverk, och så kommer det att vara en tid framöver. Bränslet som driver kärnkraftverken är ganska harmlöst att hantera innan det används i kärnkraftsreaktorerna, men efter det har använts, när det inte längre fungerar som bränsle, är det mycket farligt. Det använda kärnbränslet sänder ut stora mängder strålning av olika slag, och det kommer fortsätta att sända ut mer strålning än vad det gjorde innan det användes som bränsle länge, under så lång tid som 100 000 år. För att försöka hålla det använda kärnbränslet borta från människor under så lång tid har man tänkt sig att gräva ner det, 500 m ner i urberget.

Det finns andra problem med det använda bränslet än att det sänder ut strålning och är farligt att vara i närheten av. Några av ämnena som har bildats under tiden bränslet har varit i kärnreaktorerna kan användas som sprängmedel i kärnvapen och så kallade smutsiga bomber.

Bland annat därför är det viktigt att veta exakt vad det är man gräver ner i marken, så att inga av dessa farliga ämnen sprids i världen och kan, direkt eller indirekt, orsaka skada. För att få reda på vad det använda bränslet innehåller har man tänkt att (i kombination med andra mätmetoder) mäta neutronstrålningen från det använda kärnbränslet. Utvecklingen av ett neutrondetektorsystem för detta ändamål är vad detta examensarbete handlar om.

Det svåra i det här fallet är att det finns så mycket mer än neutroner som strålar ut från kärnbränslet än neutroner. Man måste därför kunna se skillnad på olika partiklar som skulle kunna komma att träffa detektorsystemet. För att förstå hur man kan göra detta måste vi först lära oss lite mer om neutroner.

Ja vad är neutroner nu då egentligen? Jo, det är små partiklar som tillsammans med protoner bygger upp kärnan av atomer, som i sin tur bygger upp vår värld. Neutroner, till skillnad från protoner som är positivt laddade, saknar elektromagnetisk laddning vilket gör dem svåra att upptäcka. Så för att veta när man hittat en neutron så måste man använda lite knep. Till exempel kan man få den att skapa en kärnreaktion tillsammans med någon typ av atomkärna, och genom att titta på energin som frigörs i kärnreaktionen kan man se att man har hittat en neutron.

I den kärnreaktion som används i detta examensarbete för att hitta neutroner skickas både en partikel och dessutom oftast en energirik foton, en gammafoton, ut. Om man lyckas se både partikeln och gammafotonen från kärnreaktionen samtidigt, så kan man ta bort mycket av bakgrundsaktiviteten från andra sorters partiklar, och bara titta på neutronsignalerna som är det vi är intresserade av.

Abbreviations

ADC	Analogue to Digital Converter
Amp	Amplifier
APD	Avalanche PhotoDiode
CFD	Constant Fraction Discriminator
ESS	European Spallation Source
FWHM	Full Width at Half Max
LAAPD	Large Area Avalanche PhotoDiode
LIBAF	Lund Ion Beam Analysis Facility
ND	Neutral Density
NIM	Nuclear Instrumentation Module
P420	PreLude 420
Preamp	Preamplifier
PMT	PhotoMultiplier Tube
PSD	Pulse Shape Discrimination
PVT	PolyVinylToluene
QDC	Charge to Digital Converter
SCA	Single Channel Analyser
SKB	Svensk Kärnbränslehantering AB (The Swedish Nuclear Fuel and Waste Management Company)
TDC	Time to Digital Converter
TCF	True Constant Fraction

Contents

1	Introduction	1
1.1	Method of thermal neutron detection	2
1.2	Goals and ambition	3
1.3	The contents of this thesis	3
2	Physical concepts and other relevant descriptions	4
2.1	Particle-matter interactions	4
2.1.1	Boron-10 neutron capture reaction	4
2.1.2	Photon interactions	5
2.1.3	Ion interactions	7
2.2	Particle detection with scintillators	7
2.2.1	Organic scintillators	8
	Organic scintillator types used	9
2.2.2	Inorganic crystal scintillators	9
	Inorganic scintillator materials used	10
2.3	From scintillator to energy histogram	10
2.3.1	Photomultiplier tubes	10
2.3.2	Avalanche photodiodes	12
2.3.3	Pulse processing components	12
2.4	Radiation sources	14
2.4.1	Plutonium-Beryllium	15
2.4.2	Caesium-137	15
2.4.3	Cobalt-60	15
2.4.4	Sodium-22	15
2.4.5	Thorium-228	16
3	Boron Carbide Coated Scintillators	17
3.1	Temperature sensitivity	18
3.2	Black surface of the scintillator	19
3.2.1	Black surface relation to light output	19
3.3	Aluminium coated plastic scintillator	23
3.4	Potentially damaged surface layer of plastic under boron coating	26
4	Photomultiplier Tubes or Avalanche Photo Diodes	30
4.1	The APDs	30
4.2	The PMTs	32
4.3	Resolution	32
4.4	Neutron measurements with APD	34

5	Boron loaded plastic together with an inorganic crystal scintillator	38
5.1	CsI(Tl) crystal measurements	39
5.1.1	The CsI(Tl) crystals	39
5.1.2	Coincidence measurements with CsI(Tl) and BC-454	40
5.2	PreLude 420 crystal measurements	45
5.2.1	The P420 crystal	45
5.2.2	Coincidence measurements with P420 and BC-454	46
5.3	Scintillators mounted on the same PMT	49
5.3.1	Pulse shape discrimination	49
5.3.2	CsI(Tl) and BC-454 on the same PMT	50
5.3.3	P420 and BC-454 on the same PMT	54
6	Boron Carbide Coated Diodes	60
6.1	Thorium spectra	60
6.2	Thickness of coating layer	61
6.3	Neutron measurement	63
7	Summary of conclusions and Outlook	65
	Bibliography	67

Chapter 1

Introduction

In march 2011 The Swedish Nuclear Fuel and Waste Management Company, SKB (Svensk Kärnbränslehantering AB), applied to Mark- och miljödomstolen (eng. The Land and Environmental Court) for permission to use existing and build new structures in a connected system for long term deposition of nuclear waste [1]. The structures for the long term deposition system include the existing Central Interim Storage Facility for Spent Nuclear Fuel (Clab), the planned nuclear fuel encapsulation facility as an extension to Clab (which then will be called Clink) and also the spent fuel repository as a final storage facility for nuclear waste [2].

The model used in Sweden of how to manage the nuclear waste is called KBS-3 (KärnbränsleSäkerhet, eng. nuclear fuel safety) [3]. The concept was created in 1983 as a part of an application by SKBF (now SKB) to be allowed to load fuel in the reactors Forsmark 3 and Oskarshamn 3, and it has been duly modernised over the years [2, 3].

The principle of the management concept is the following. The nuclear waste will first be stored at the power plants for some time in water tanks, before it is shipped to interim storage at the Clab (Clink) facility where it will be kept in water pools for about 30 years [2]. After this the fuel is supposed to be encapsulated in copper canisters, five metres long and with a weight of 25 metric tonnes when filled, before being put in the spent fuel repository [4]. This repository will be situated at a depth of about 500 m under ground in the bedrock [4], where there will be a layer of bentonite clay between the copper and the bedrock [4]. The nuclear waste will then be protected behind many barriers, intended to be enough to protect the material for 100000 years, which is the approximate time needed to reduce the wastes radiotoxicity to the same level as natural uranium and the time the nuclear waste is supposed to be stored in the repository [2, 4].

Before the nuclear waste is deposited in its final resting place, it needs to be established what is being sent down into the repository. The perhaps most essential issue when dealing with active nuclear material, after the safety of people in the proximity of the material of course, is the non-proliferation of the isotopes possible to use in nuclear weapons. Those isotopes do exist in spent

nuclear fuel. The point of measuring the contents of the copper canisters is thus to investigate what is in them, and that nothing that is supposed to be in them is missing. In the IAEA Safety Standards for the Storage of Spent Nuclear Fuel [5] it is said that *“The operating organization will be required to establish, maintain and implement a system for nuclear material accounting and control...”* for this reason.

To be able to investigate the content of the spent nuclear fuel waste capsules a method including the detection of the thermal neutron radiation from the copper canisters is suggested. This master thesis project is about developing this neutron detection system, as the title suggests.

1.1 Method of thermal neutron detection

Over the last few years there has been a large number of reports, papers and documents related to neutron detection which has started with the words “Due to the ^3He crisis...” or equivalent. This crisis has its root in the recent decrease in accessibility of ^3He on the market, and has led to an increase in research regarding alternative ways to detect neutrons.

The nuclear weapons programme of the USA has indirectly generated a large amount of ^3He by the decay of tritium (^3H) used in some types of the nuclear warheads they maintain [6]. The tritium is kept in a gas mixture with deuterium in a container just outside the plutonium or uranium containing fission-part of the warhead. As the fission is induced, the tritium and deuterium gas mixture is compressed and heated, which starts so called D-T (Deuterium-Tritium) fusion reactions. The fusion reaction results in one ^4He nucleus being created along with a high energy neutron. This neutron can induce further fission reactions in the uranium or plutonium, increasing the rate of fissions in the bomb and lets more fissions take place before it explodes which makes it more powerful.

Since the ^3H decays into ^3He , the ^3He needs to be extracted and more ^3H filled into the warheads. The ^3He has up till recently been sold on the market, making it possible to be used for scientific and industrial purposes. However, recently the government in the USA have started to use ^3He -based neutron detectors at their borders as a means to detect smuggled fissile material which has greatly reduced the supply of ^3He [6].

Neutron detectors based on ^3He has been common because of its large reaction cross section with neutrons. Since there is no or limited supply of ^3He , other means of neutron detection must be utilised. The boron isotope ^{10}B is an attractive option to use, since it also has a quite large reaction cross section with neutrons, though not as large as ^3He . It is ^{10}B that will be used in this project to detect thermal neutron radiation in the form of ^{10}B doped plastic scintillators.

When a neutron is absorbed by a ^{10}B nucleus an alpha particle and a lithium ion is released, which often is in an excited state. The lithium ion de-excites by releasing a photon. By detecting the reaction products and the photon simultaneously, a lot of background noise can be removed and the neutron event

can be defined with more confidence. This is the idea behind neutron detection that will be used in this thesis.

1.2 Goals and ambition

Going into this project the goal was to develop and construct a detector system for measurement of thermal neutron radiation from spent nuclear fuel. This has not changed in the duration of the project.

There is also an ambition to incorporate a possibility to measure the full gamma radiation spectrum from the spent fuel as well as fast neutrons to be able to get a more complete picture of the spent fuel. If there was time this would have been introduced during this project. This was not the case, so this thesis will be restricted to the detection of thermal neutrons.

1.3 The contents of this thesis

This thesis will in Chapter 2 be started with an introduction to the physical concepts which lie behind the experiments conducted. The chapter includes the most relevant particle interactions with bulk material, and means of particle detection including scintillators, signal amplification and pulse processing.

After this follows a description of boron carbide coated scintillators along with discussion about the challenges connected with those in Chapter 3. Boron carbide coated scintillators are of interest because they can be made very thin without loss of effectiveness, and thereby be fairly non-sensitive to gamma radiation.

Chapter 4 include a discussion of the use of photomultiplier tubes versus avalanche photodiodes. Avalanche photodiodes are much smaller devices than photomultiplier tubes which makes them interesting.

The meat and potatoes of this thesis so to speak will be presented in Chapter 5. There neutron detector systems are described that use a boron loaded plastic scintillator along with a gamma ray detecting inorganic crystal scintillators used to detect the photon released in the ^{10}B nuclear reaction with a thermal neutron.

An interesting sidetrack presenting an alternative means of neutron detection will be discussed in Chapter 6. The idea presented there is that photodiodes are coated with boron carbide for direct detection of the charged particles resulting from the ^{10}B reaction with a neutron.

For last, in Chapter 7, the discussion about the different parts of this project will be summarised for a condensed presentation of what is learned from this project. Based on this discussion an outlook toward the future will be presented.

Chapter 2

Physical concepts and other relevant descriptions

For the reader familiar with radiation detection and nuclear physics this chapter can be skipped without any loss. For the more novel reader it can be a good idea to skim this through and read the paragraphs and sections that concerns unfamiliar subjects.

This chapter is not intended to be an advanced and heavy theoretical description of all physical phenomena related to this project. It is designed to illuminate some of the more important parts of this thesis and to provide sufficient knowledge such that the reader may be able to grasp what lies behind the reasoning and results presented here.

2.1 Particle-matter interactions

The way different particles interact with matter is of course an essential subject when trying to detect particles. The particles of interest here are neutrons, photons, and ions (protons, alpha particles and heavier ions), and the manner of their interaction will be presented here in a more or less brief way.

2.1.1 Boron-10 neutron capture reaction

First and foremost the basis of the neutron detection method used in this project is described. The isotope ^{10}B can undergo the reaction $^{10}\text{B}(n, \alpha)^7\text{Li}$ when an incident neutron collides with a ^{10}B nucleus. An equivalent way to write this is



where Q is the energy released in the nuclear reaction.

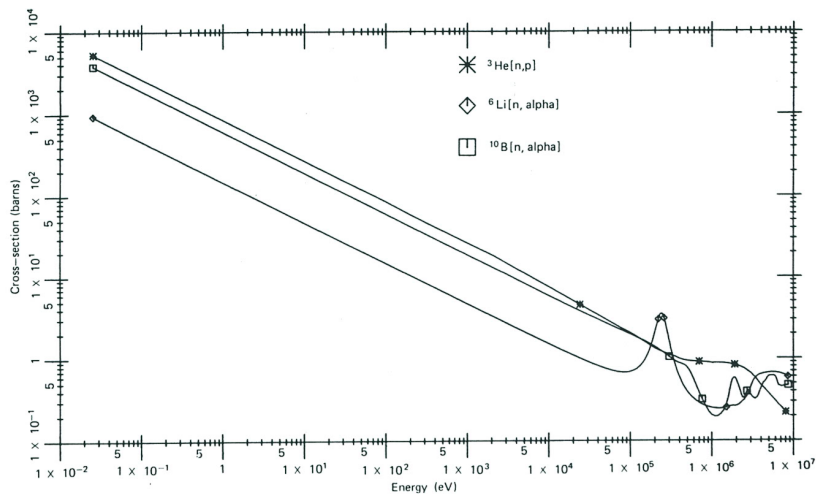


Figure 2.1: The neutron capture reaction cross section for ${}^3\text{He}$, ${}^6\text{Li}$ and ${}^{10}\text{B}$ as a function of neutron energy. Picture from Glenn F. Knoll, Radiation detection and measurement [7].

The resultant ${}^7\text{Li}$ nucleus of the reaction in Equation 2.1 can be either in its ground state with a 6 % probability, or its lowest excited state with a 94 % probability [7]. The Q-values for these reactions are 2.792 MeV and 2.310 MeV for the ground state and the excited state branch respectively [7]. The excited ${}^7\text{Li}$ nucleus (often written ${}^7\text{Li}^*$) decays to the ground state by emitting a 478 keV photon [8].

The large Q-value relative to the incident thermal neutron energy and presumably also the energy of the boron atom makes it possible to with good accuracy approximate the kinetic energy of the reaction products to solely originate from the energy of the reaction Q-value. One can therefore also approximate the linear momentum (mass \times velocity) of the system as being zero. Then the energies of the reaction products are 1.47 MeV for the alpha particle and 0.84 MeV for the ${}^7\text{Li}$ ion if the ${}^7\text{Li}$ is taken to be in the excited state [7].

The cross section for this reaction is 3840 b (b = barn = 10^{-28} m²) for thermal neutrons (i.e. with an energy of ~ 0.025 eV) [7]. Figure 2.1 shows the reaction cross section for this and two other neutron capture reactions as a function of neutron energy. 3840 b is a quite large reaction cross section which makes this reaction an attractive option to utilise.

Alternative ways to detect neutrons is to use other nuclear reactions (e.g. with ${}^3\text{He}$ or ${}^6\text{Li}$), or scatter neutrons on e.g. protons and detect the energy of the recoiled particles. Here only the ${}^{10}\text{B}$ reaction is considered.

2.1.2 Photon interactions

Concerning the interactions between photons and matter one usually mention three types of interactions (at least in relation to gamma radiation measure-

ments): the photoelectric absorption (photoelectric effect), Compton scattering (or inelastic scattering) and pair production. These phenomena will be described briefly here, and are described more fully in e.g. [7, 9, 10].

In the photoelectric effect a photon is absorbed fully by an atom. All energy in the photon is taken by an electron in some atomic shell, and the electron may be released as a photoelectron if the energy of the absorbed photon is larger than the electron binding energy. This is generally the case for photons in the gamma ray regime. The probability of photoelectric absorption increases with the atomic number Z of the target material. Therefore a high- Z element is beneficial if photoelectric absorption is sought, which it often is since all the energy of the photon is absorbed in the process.

Compton scattering is the process where a photon transfers some of its energy to an atomic electron by scattering against it. The amount of energy transferred depends on the scattering angle of the photon according to Equation 2.2 [7].

$$E' = \frac{E}{1 + \frac{E}{m_0 c^2} (1 - \cos \theta)} \quad (2.2)$$

E' is the energy of the photon after scattering, E before scattering, m_0 is the rest mass of the electron, c is the speed of light in vacuum and θ is the scattering angle. The smallest amount of energy will be transferred from the photon if the scattering angle θ is very small, and the largest amount of transferred energy possible will be for $\theta = \pi$ and the photon is scattered backwards from where it came. This energy is the backscattering energy

$$E_{back} = \frac{E}{1 + \frac{2E}{m_0 c^2}} \quad (2.3)$$

In a radiation detector the Compton scattering process will give rise to a continuum of detected energies, for all of the possible scattering angles. The deposited energy of a Compton scattered photon is

$$E_{dep} = E - E' = E \frac{\frac{E}{m_0 c^2} (1 - \cos \theta)}{1 + \frac{E}{m_0 c^2} (1 - \cos \theta)} \quad (2.4)$$

The maximal energy $E_{dep}|_{\theta=\pi} = E_{CE}$ will be represented as an edge in the radiation detector which is called the Compton edge. This energy is thus

$$E_{CE} = E \frac{\frac{2E}{m_0 c^2}}{1 + \frac{2E}{m_0 c^2}} \quad (2.5)$$

Pair production can occur close to the nucleus of an atom. This effect will not be discussed or considered further in this work, but is mentioned here in short for the sake of completeness. What happens is that an incident photon is transformed into an electron positron pair. The positron disintegrates subsequently with an electron and creates two disintegration quanta, which are photons with

an energy of 511 keV each emitted back to back. 511 keV is also the mass energy (m_0c^2) of an electron and a positron, which means that the energy of the incident photon needs to be larger than 1022 keV for this process to be able to happen.

2.1.3 Ion interactions

Ions impinging on a material will interact with it by means of coulomb interaction, i.e. electromagnetic attraction and repulsion to the electrons and nuclei within the target material. Mainly the interaction will be with the electrons, and not so much with the nuclei [7]. This is because the target material is generally made up of neutral atoms with no net charge. The nuclei of the target material will be screened of by the negative charge of the electron shell. This negative charge will be what an outside viewer, like the ions, mainly experiences and interacts with.

The passing ions will disturb the orbital electrons and transfer some of their energy, exciting electrons or ionizing atoms in the wake of the ions. How much energy is transferred from the ion to the material is described by the linear stopping power S , defined in Equation 2.6 [7].

$$S = -\frac{dE}{dx} \quad (2.6)$$

Here dE is the differential energy loss and dx is the differential path length. This parameter may be described in terms of properties of the impinging ion and the target material, for instance by the so called Bethe formula. This is not done in this report however.

The energy loss of an ion in a thin layer of a material is then given by Equation 2.7. Here t is the thickness of the layer and $-\left(\frac{dE}{dx}\right)_{avg}$ is the average linear stopping power of the layer.

$$\Delta E = -\left(\frac{dE}{dx}\right)_{avg} t \quad (2.7)$$

2.2 Particle detection with scintillators

Scintillators are pieces of material that re-emits energy deposited into them as bursts of light, i.e. scintillations. The light is usually in the visible spectrum and the amount of it should for a good scintillator be proportional to the amount of energy deposited. The scintillator should not absorb the light it sends out itself either.

The scintillation light can be transformed to electrons by means of a photocathode or similar, and the electrons in turn can be multiplied to form a readable current. This current would be proportional to the energy that the incident particle has transferred to the scintillator material, and an energy spectrum of particles could be created. More about this procedure in Section 2.3.

Energy deposited in the material is quickly released by scintillations. The energy re-emission process can be approximated as in Equation 2.8 [9]

$$N = \frac{N_0}{\tau_d} e^{-\frac{t}{\tau_d}} \quad (2.8)$$

where N is the number of photons released at time t , τ_d is the decay constant and N_0 is the total number of photons released. This approximation is valid if the rise time of the system is much shorter than the decay time [9], where the rise time is the time it takes for the incoming energy to excite the atoms of the scintillator material and the decay time the time it takes for them to relax (which is described by the decay constant). For a non-negligible rise time the expression is changed into

$$N = N_0 f(\sigma, t) e^{-\frac{t}{\tau_d}} \quad (2.9)$$

where f is a Gaussian that needs to be determined experimentally [9].

The scintillations of the material in the scintillator may be emitted not only by one type of decay, but originate from different processes of the molecules, atoms and the crystal structures [9]. How fast these decay processes are, differ among them and between materials. It is therefore possible, usual even, that the radiation re-emission of a scintillator can better be described as a sum of exponentials as in Equation 2.10 than in Equation 2.8.

$$N = A_1 e^{-\frac{t}{\tau_1}} + A_2 e^{-\frac{t}{\tau_2}} + \dots \quad (2.10)$$

Here A_i is the relative magnitude and τ_i is the decay constant of the component i .

Since the decay times are depending on physical properties of the material, the manner of how the material is excited will matter in regards to how scintillation light is emitted from the material. A photon with the same energy as an alpha particle that is captured in the scintillator may thus result in different responses from the scintillator in a timing sense, but also in the amount of light released. A particle which results in a lower light output even though it has deposited the same energy is quenched. The material is in that case excited in a way that it may relax without releasing scintillation light.

2.2.1 Organic scintillators

The organic scintillators come in the form of crystals, liquids or plastics. The organic material consists of many light elements, such as hydrogen and carbon, which sets the physical properties of the scintillators. These scintillators have in general a quite fast timing properties and low light yield [7].

Table 2.1: Properties of plastic scintillators

	BC-400	BC-404	BC-440	BC-440M	BC-454
Light output (% of Anthracene)	65 ^a	68 ^a	60 ^b	60 ^b	48 ^c
Decay Time (ns)	2.4 ^a	1.8 ^a	3.3 ^b	3.3 ^b	2.2 ^c
Softening point (°C)	70 ^a	70 ^a	99 ^b	150 ^{b*}	60 ^c
Wavelength of emission maxima (nm)	423 ^a	408 ^a	434 ^b	434 ^b	425 ^c

^a from [11], ^b from [12], ^c from [13], * Not an actual softening point, but rather the highest recommended temperature of use [12]

Organic scintillator types used

The types of organic scintillators used in this project are plastic ones based on the material polyvinyltoluene (PVT) [11–13]. Some of their properties are listed in Table 2.1.

Noticeable is the short decay time of the BC-404 scintillator which then is suitable for a fast counting system, and the BC-440 and BC-440M models that have a higher temperature tolerance. The BC-454 one is loaded with boron. The doping concentration is 5 % by mass. The dopant is natural boron, which in turn consist of 19.9 % ¹⁰B, which makes it sensitive to neutrons according to Equation 2.1.

The doping also makes the light output decrease. This happens because the impurities in the otherwise scintillating material introduce ways for the scintillator material to relax without sending out scintillation light. Thus the amount of boron introduced, and by that the neutron detection efficiency, needs to be balanced against the light output of the scintillator.

2.2.2 Inorganic crystal scintillators

The inorganic scintillators have generally longer response time than the organic ones, but exactly how long differs greatly from case to case. Between some hundredths of nanoseconds up to a few microseconds are common [7]. The inorganic scintillators are often sensitive to water [9], even the humidity in air could be harmful which increases the difficulty in handling the scintillators. This property of the material is called its hygroscopicity. Depending on the application this might be an important feature to consider.

These types of scintillators do often contain many heavy elements which gives larger stopping power of particles and a larger cross section for photoelectric absorption. They have in general quite high light output and therefore good energy resolution.

Table 2.2: Properties of inorganic scintillator materials [14]

	CsI(Tl)	PreLude 420	BGO [*]	YAG [*]
Decay time (ns)	1000	41	300	70
Light yield (photons/keV)	54	32	8-10	8
Light output (% of NaI(Tl) in a bialkali PMT)	45	75	20	15
Density (g/cm ³)	4.51	7.1	7.13	4.55
Wavelength of emission maxima (nm)	550	420	480	550

^{*} Not delivered in time to be tested

Inorganic scintillator materials used

The materials that will be used in measurements in this project is $\text{Lu}_{1.8}\text{Y}_{0.2}\text{SiO}_5$ (PreLude 420 from Saint-Gobain, or short P420) and CsI(Tl) (thallium doped caesium iodide). There were other candidates that was ordered, but long delivery times excluded them from this thesis. Those were $\text{Bi}_4\text{Ge}_3\text{O}_{12}$ (bismuth germanate, BGO) and $\text{Y}_3\text{Al}_5\text{O}_{12}(\text{Ce})$ (cerium doped yttrium aluminium garnet, YAG(Ce)). The two scintillator materials that were used have properties that will make them interesting to compare with each other. They have for instance widely different decay times, which is interesting in terms of pulse shape analysis. They also contain elements with a high Z content for high photoabsorption. The CsI(Tl) scintillator is slightly hygroscopic, but is not that sensitive compared to others. Some properties of the scintillator materials is presented in Table 2.2, obtained from [14].

2.3 From scintillator to energy histogram

As was mentioned in Section 2.2 the created scintillations needs to be transformed to electric signals to be of good use. Therefore, in direct contact with the scintillator there is usually a so called photomultiplier tube (PMT).

2.3.1 Photomultiplier tubes

The function of a PMT is to translate the incoming photons, from e.g. a scintillator, into a current. The resulting current is ideally proportional to the energy of the photons that hit the PMT which in turn should be proportional to the energy of the incoming particle to the scintillator.

Incoming photons illuminating the PMT first hit a photocathode that subsequently sends out an electron with some probability. This probability is expressed in the useful quantity called quantum efficiency which is defined in

Equation 2.11 [9].

$$\eta(\lambda) = \frac{\text{number of photoelectrons released}}{\text{number of incident photons on cathode}(\lambda)} \quad (2.11)$$

Here λ is the wavelength of the incoming light. Since the quantum efficiency depends on the wavelength of the light, different scintillators can preferably be used with a photocathode with a high quantum efficiency at the wavelengths emitted by the scintillator.

The released electrons from the photocathode is then lead into a series of so called dynodes which amplify the electron current. There are several ways these dynodes can be oriented in with respect to one another, each configuration with its own name and with certain advantages.

At the dynodes the number of electrons will increase by a certain amount called the secondary emission factor δ which depends on the energy of the electron released by the photocathode. In a series of n dynodes with a potential difference V_d in between them the secondary emission factor can be written as

$$\delta = KV_d \quad (2.12)$$

where K is some proportionality factor, and the total gain of the PMT is

$$G = \delta^n. \quad (2.13)$$

If the PMT is connected to a scintillator with decay constant τ_d , the current out from the PMT resulting from an event in the scintillator is

$$I(t) = \frac{GNq_e}{\tau_d} e^{-\frac{t}{\tau_d}} \quad (2.14)$$

where N is the number of electrons emitted by the photocathode and q_e is the elemental charge.

The PMT can be represented in terms of circuit components as a current generator, coupled parallel with a resistance R and a capacitance C [15]. The current can in that case be expressed as

$$I(t) = \frac{V}{R} + C \frac{dV}{dt} \quad (2.15)$$

where V is the electric potential. The potential can be solved for from Equations 2.14 and 2.15 as

$$V(t) = \begin{cases} -\frac{GNq_e R}{\tau - \tau_d} (e^{-\frac{t}{\tau_d}} - e^{-\frac{t}{\tau}}) & , \tau \neq \tau_d \\ \frac{GNq_e R}{\tau} t e^{-\frac{t}{\tau_d}} & , \tau = \tau_d \end{cases} \quad (2.16)$$

where $\tau = RC$ [9].

2.3.2 Avalanche photodiodes

There are alternatives to the PMT. One is the Avalanche PhotoDiode (APD). In a PMT the incident photons are converted to electrons by means of a photocathode, whereas in the case of the APD this is done by a photodiode. The diode is reverse biased, and utilise the avalanche effect of a reverse biased semiconductor junction for charge carrier multiplication.

Ordinary photodiodes (with no avalanche) is commonly used as a tool of detecting photons and charged particles. A diode is made up of semiconductor material, and one side of the diode has a surplus of electrons and the other has an electron shortage. There is then an electric field created between the two sides. One may then apply a voltage over the region that has an electric field and which has been depleted from space charge (the depletion region) to increase the electric field strength. This is called to apply a reverse bias.

A charged particle or a photon that is introduced in the depletion region may there excite an electron up to the so called conduction band. The electron and the hole left by the electron in the so called valence band whence it came is then affected by the electric field and is accelerated, thereby creating a measurable current.

The difference between a regular diode and an APD is the magnitude of the reverse bias applied. The avalanche photodiode requires a much larger bias than the regular photodiode to operate properly. This is because the APD uses the so called avalanche effect. When an electron in the conduction band is swept by the electric field, it may if the bias is large enough in turn excite more electrons, and so on, creating an avalanche.

By this means, even a single photon that is absorbed in the APD might give a large enough signal that can be processed. This makes the APD an interesting device to utilise.

2.3.3 Pulse processing components

After the initial production of an electronic pulse that is related to the detected particle energy, the pulse is processed with the goal to read out this energy in some manner. Usually as data collected in a computer. A few examples of what the pulse processing modules used may look like is seen in Figure 2.2. The ones seen in the photograph are of the so called NIM standard (Nuclear Instrumentation Module).

Often the signal from the detector is weak. Sometimes it is not, but if it is one would like to amplify the weak detector signal into something tangible. This is done by a preamplifier (preamp). The amplification from a preamp is linear, i.e. the pulse shape of the output pulse is the same as that of the input pulse. The height of the output pulse from the preamp is proportional to the charge that is released at the end of the detector as a result of the incident radiation to it. This pulse has in general a steep rising edge and a exponentially decreasing tail back to the zero level. How long this tail is depends on the detectors decay time.



Figure 2.2: A few modules used for processing of pulses from detectors

There are a few different alternatives of what to do with the pulse from the preamplifier. One possibility is to send the pulse to a shaping amplifier (or just amplifier or amp for short). This unit integrates (and differentiates) the pulse from the preamp and sends out a pulse with a Gaussian shape, where the height is proportional to the charge released from the detector.

The pulses coming from the amplifier can then be analysed in terms of their height, and thus the energy of the particles which initiated the pulse in the first place, by an Analogue to Digital Converter (ADC). This unit makes a digital signal output based on the height of the pulse from the amplifier, i.e. makes a binary signal that says what energy the particle that hit the detector had.

One alternative path after the preamplifier stage is to send that signal to a charge (Q) to Digital Converter unit (QDC). Here the pulse is integrated, and a digital signal which is proportional the charge from the detector is created directly.

There are yet other options what to do with a preamplifier pulse. It is becoming more and more common to digitise the whole pulse from the preamp and store it as the data from the measurements. It is then possible to manipulate the pulse by means of software in different ways which can be much more versatile than using analogue electronic modules.

The ADC and QDC units needs a logic (square) trigger pulse to know when to look for a peak or when to integrate the incoming signal. This pulse is commonly generated by sending a copy of the preamp pulse to a discriminator unit.

The copy of the pulse is created in a so called fan unit; usually a fan-in/fan-out which can sum incoming pulses and create several identical output signals. When one of these copies reaches a discriminator unit, this unit will send out a logic signal if the amplitude of the incoming pulse is larger than a certain pre-set value. This type of discriminator is called an integral discriminator.

Another type of discriminator, frequently used in this project, is the Constant Fraction Discriminator (CFD). This type of discriminator sends out a logic pulse when the incoming pulse has reached a certain fraction of its maximum height.

For pulses with the same shape but different amplitudes the output of an integral discriminator would be generated at different times compared to the origin of the pulse. This time difference is called the time walk. For a CFD this is not the case since the rise time of the pulse to a constant fraction of its maximum height is the same, independent of the absolute height of the pulse.

The input signal to the CFD is duplicated, and one of the signals is inverted, attenuated and delayed a chosen time. The signals are then summed and the CFD sends an output signal at the zero crossing of the summed pulse, which would be at a constant fraction of the maximum pulse height.

The characteristics of the incident pulses in terms of rise time determines how the signal from the CFD should be formed. On the unit used (Tennelec TC 454 Quad CFD) a delay cable should be connected between two front side ports. The delay of the cable is added to the internal delay that in this case is $t_{internal} = 0.6$ ns [16].

What is called true constant fraction (TCF) mode is desirable mainly in fast timing applications. In this mode the zero crossing is simultaneous with the peak of the inverted, delayed and attenuated signal. For this to work well the rise time of the pulses need to be similar, but the amplitudes can vary. A rule of thumb regarding the pulse delay in the TCF mode is given in Equation 2.17 [16].

$$t_{delay} = t_{rise}(1 - f) \quad (2.17)$$

Here $t_{delay} = t_{cable} + t_{internal}$ is the delay time of the delayed pulse, t_{rise} is the rise time of the incoming pulse, and f is the constant fraction discriminated at as well as the attenuation factor of the delayed pulse. For the unit used $f = 0.2$.

There is another type of module of interest which digitises the signal. This is called the Time to Digital converter (TDC). The type of TDC used here records the time difference between incoming logic pulses and a trigger pulse during a time window before the trigger pulse has arrived. This can be used for instance to keep track of when signals from discriminators arrives in relation to each other.

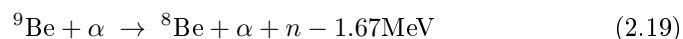
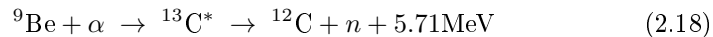
A few more types of modules were used during the measurements. Significant ones not described here will be explained in sufficient detail at the point knowledge of them is important.

2.4 Radiation sources

A few types of radiation sources was used for calibration measurements and other trials. The manner of the activity of the sources and the energies of the main particle emissions from them will be given in this section.

2.4.1 Plutonium-Beryllium

Only one type of neutron source was used, namely Plutonium-Beryllium (PuBe). Some isotopes in the plutonium decay chain decays by alpha decay. Alpha particles can be absorbed by the beryllium isotope ^9Be , and produce neutrons by the reactions displayed in Equations 2.18 and 2.19 [17].



Reactions of the type $(n, 2n)$ are also possible, as are neutron induced fission of e.g. Pu isotopes which can produce multiple neutrons [17] (self multiplication).

There is also a rather large amount of gamma radiation emitted by the PuBe source. The exact composition of that will not be discussed.

2.4.2 Caesium-137

Caesium-137 (^{137}Cs) is used as a gamma radiation source. It decays by β^- -decay [18]. 94.4 % of the decays leaves a ^{137}Ba nucleus in an excited state and 5.6 % a ^{137}Ba nucleus in the ground state [18]. The excited state is 0.661 MeV above the ground state in energy [18] and decays by gamma emission.

2.4.3 Cobalt-60

There are three excited states in ^{60}Ni to which cobalt-60 ^{60}Co decays by β^- -decay [19]. The pre-eminent alternative is the energy level highest in energy, 2.506 MeV above the ground state to which 99.8 % of the decays go [19]. From this state the nucleus usually (in more than 99 % of the cases [19]) decays in two steps: first by emission of a 1.173 MeV gamma photon and subsequently a 1.333 MeV photon [19].

2.4.4 Sodium-22

The isotope sodium-22 (^{22}Na) is used as a gamma radiation source and decays by β^+ -decay or electron capture (EC) to an excited state of neon-22 (^{22}Ne) in almost all cases. Only 0.056 % of decays end up directly in the ground state [20]. The excited state decays to the ground state by emitting a 1.275 MeV photon [20]. If the decay to ^{22}Ne is by beta decay, two annihilation photons of 0.511 MeV each is produced when the positron created in the beta decay annihilates with an electron.

2.4.5 Thorium-228

^{228}Th is the only alpha particle source used. It is part of a decay chain which includes a number of α -decays. The main decay alpha particle energies are 5.423 MeV (in 73.4 % of cases) or 5340 MeV (26.0 %) from ^{228}Th [21], 5.685 MeV from ^{224}Ra [22], 6.051 MeV from ^{212}Bi [23], 6.288 MeV from ^{220}Rn [24], 6.778 MeV from ^{216}Po [25] and 8.785 MeV from ^{212}Po [26].

Chapter 3

Boron Carbide Coated Scintillators

This master thesis is a part of a project which has been ongoing for a while before the author joined, and will be after his departure. Preceding the work by the author, investigations had been conducted in a bachelor thesis by Bodahl [27], where characteristics of boron carbide (B_4C) coated scintillators was investigated along with the possibility of neutron detection using a coated scintillator. Following up on this, studies were made concerning coating with boron carbide and how that affects the properties of scintillators.

The boron carbide coating is done by ESS Linköping utilising the process described by Höglund et. al. in [28]. The B_4C is sputtered onto the target by dc magnetron sputtering [28], where the target in this case is Saint-Gobain BC-440 and BC-440M plastic scintillators. The plastic scintillators used in the study by Bodahl was Saint-Gobain BC-400 and BC-404 [27]. Those scintillators have also been used for tests in this work. The plastic scintillators used are general purpose scintillators. Properties of the BC-400 and BC-404 scintillators can be found at [11], and of BC-440 and BC-440M at [12], as well as in Table 2.1.

The idea behind coating a scintillator with boron carbide is that an incident neutron shall interact with the boron in the coating. The alpha particle may then enter the scintillator volume and there deposit its energy. Half of the neutron interactions will not be detected because the alpha particle may be emitted in the opposite direction from the scintillator volume, and the alpha particles that enter the scintillator will have lost some energy in the B_4C layer. But there are some benefits also.

Since the neutron has already interacted, the scintillator will only need to be as thick as needed to stop the alpha particle fully. A thin scintillator will, apart from not taking up unnecessary space, not be as sensitive to gamma radiation as a thick scintillator would be. Discriminating against gamma radiation is an important aspect of neutron detectors.

There is a difference in size between the scintillator models used. The BC-400 ones are $23 \times 23 \times 3 \text{ mm}^3$, the BC-404 $23 \times 23 \times 5 \text{ mm}^3$, and the BC-440 and

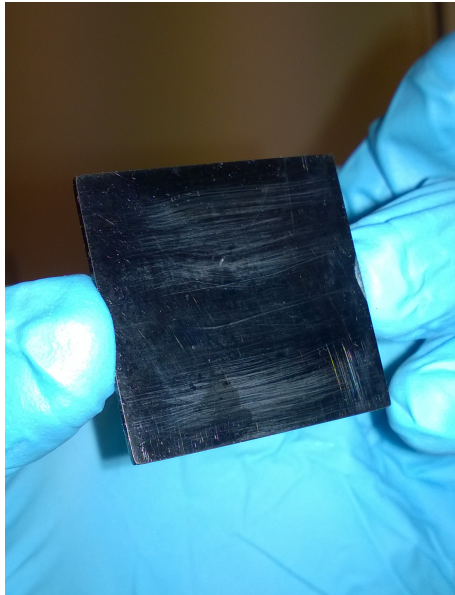


Figure 3.1: A B_4C coated BC-440M scintillator

BC-440M are $32 \times 32 \times 2 \text{ mm}^3$. Figure 3.1 shows a coated BC-440M scintillator, with the coated side facing the camera.

There are some issues coating scintillators with boron carbide, of which a few will be discussed here. Some results will be presented in a semiquantitative way, and some aspects will be discussed in a more conceptual way. The reason not everything is quantified is mostly due to the weakness of the signal from the thin plastic. It is hard to say if the signal is there at all if the conditions are anything but perfect, even more so to ascertain if it has changed slightly because of some change of parameters, and exactly how much that would be.

3.1 Temperature sensitivity

For this project, the major difference between the plastic scintillator models is their temperature sensitivity. The BC-400 and BC-404 models have a softening point of $70 \text{ }^\circ\text{C}$ [11], while the BC-440 has a softening point of $99 \text{ }^\circ\text{C}$ [12] and the BC-440M model can be used up to $150 \text{ }^\circ\text{C}$ [12]. The temperature sensitivity is important since the scintillators are exposed to rather high temperatures during the coating process. In the description by Höglund et. al. some results for deposition temperatures of $100 \text{ }^\circ\text{C}$ to $400 \text{ }^\circ\text{C}$ on aluminium alloy surfaces are presented [28]. The plastic scintillators used here are not subject to that high temperatures; the maximum temperature during the coating is measured to be $60 \text{ }^\circ\text{C}$.

Since the softening temperature of the BC-400 and BC-404 models is close to the temperature of the coating process, there may be some damages of the plastic, or rather some potential change of the properties of the scintillator. Thus a

scintillator designed to withstand higher temperatures may work better after it is coated.

However, no differences between the scintillator models could be seen that could be ascribed to temperature sensitivity. The different surface areas and scintillator volumes of the different models makes it difficult to pinpoint certain differences to originate from the temperature sensitivity of the plastic. The different plastic types were used in measurements of varying nature, both with neutron and gamma sources, but no general trend could be spotted in regards to the type of plastic used.

3.2 Black surface of the scintillator

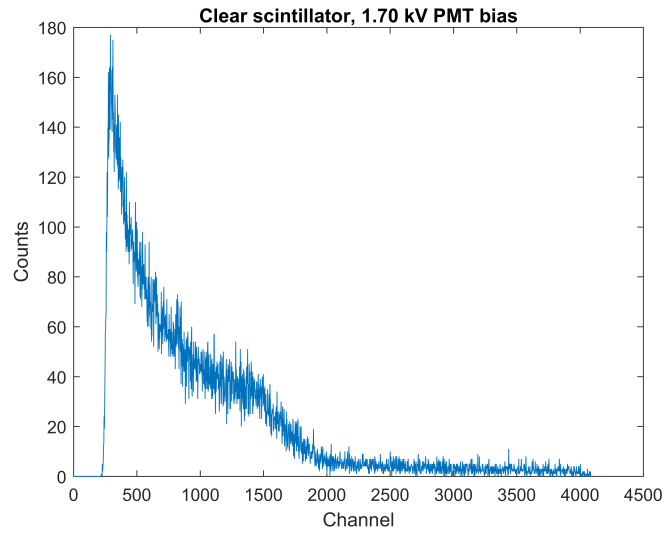
As seen in Figure 3.1 the boron carbide surface is dark, and thus absorbs much of the visible light. Such light that is emitted by the scintillators for instance. Measurements are made to determine whether the blackness of the B_4C coated surface contributes to this. A non-coated BC-404 plastic scintillator is mounted on a PMT and an energy spectrum is taken of a Cs-137 sample. This spectrum is then compared to one where the scintillator have been covered with black electrically insulating tape on the side facing away from the photocathode of the PMT. All other experimental parameters are kept the same. Differences between the spectra are then ascribed to the blackness of the surface.

Two different biases were used on the PMT for each case, both for the clear and for the blacked case, 1.70 kV and 1.80 kV respectively. The different biases are not expected to render different results, but more data can give a better idea of the contribution of the black surface.

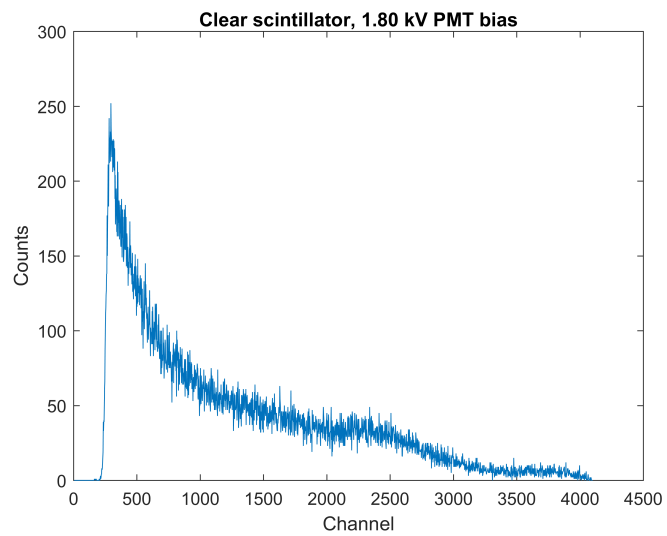
One may think that one black surface could be the cause of maximally a loss of a factor two of the scintillation light, if it is totally black. However, the light can be reflected between the surfaces of the scintillator multiple times before entering the photocathode of the PMT. Thus if one side of the scintillator is black and much of the light hitting that surface is absorbed each time, more than 50 % of the light emitted could be absorbed. On the other hand if much of the light is reflected within the scintillator a black layer outside of the plastic but in direct contact may not matter that much. Only the fraction of the light that escapes the scintillator volume and would scatter on something on the outside and then return into the scintillator would be the amount of light that could be saved if a surface with as low light absorption as possible is used in contact with the scintillator.

3.2.1 Black surface relation to light output

Energy spectra in terms of channel number are shown for two different PMT biases, 1.70 kV and 1.80 kV of a ^{137}Cs source. Figure 3.2 shows energy spectra obtained for a clear scintillator. Figure 3.2a for a bias of 1.70 kV and 3.2b for 1.80 kV. The Compton edge is ending at approximately channel 2000 in Figure 3.2a, and 3300 in Figure 3.2b.



(a) 1.70 kV



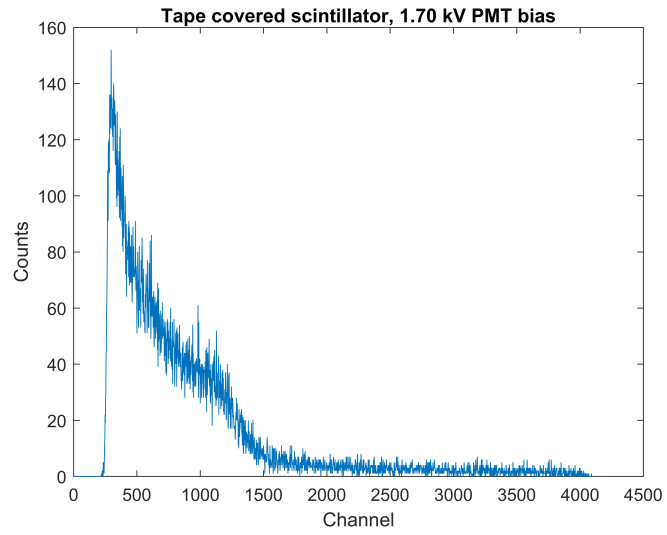
(b) 1.80 kV

Figure 3.2: Two different PMT biases for a clear scintillator, i.e. no blacked out surface

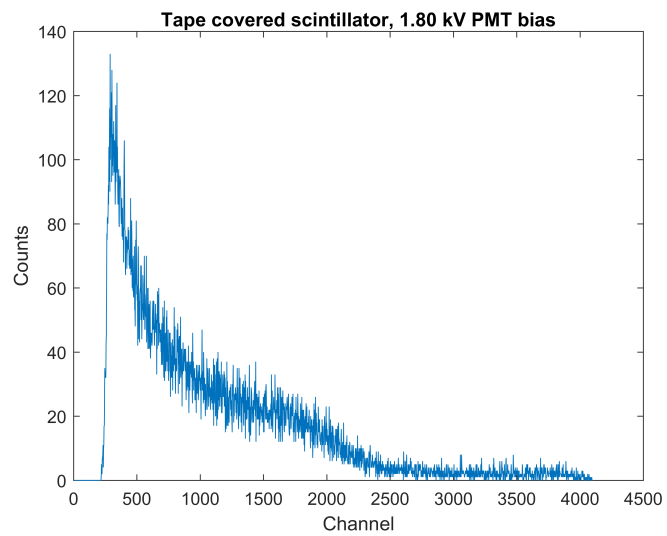
Figure 3.3 shows ^{137}Cs spectra taken by a scintillator with the side facing away from the photocathode of the PMT covered by a layer of black electrically insulating tape. Again the bias on the PMT was both 1.70 kV, Figure 3.3a, and 1.80 kV, Figure 3.3b. The Compton edge in these figures reaches approximately to channel 1550 in Figure 3.3a and to channel 2400 in Figure 3.3b.

The effect of having one surface of the scintillator black is then an energy loss of about $\frac{2000-1550}{2000} = 23\%$ for the 1.70 kV case and $\frac{3300-2400}{3300} = 27\%$ for the 1.80 kV case. Thus one can say that about a quarter of the scintillation light is lost when having a black tape surface instead of a clear one.

In Section 3.4 another experiment is conducted, where this phenomenon is discussed further. There it would seem that the loss of scintillation light is even larger than this for a scintillator coated with B_4C .



(a) 1.70 kV



(b) 1.80 kV

Figure 3.3: Two different PMT biases for a black surface scintillator, i.e. one side blacked out by electric tape

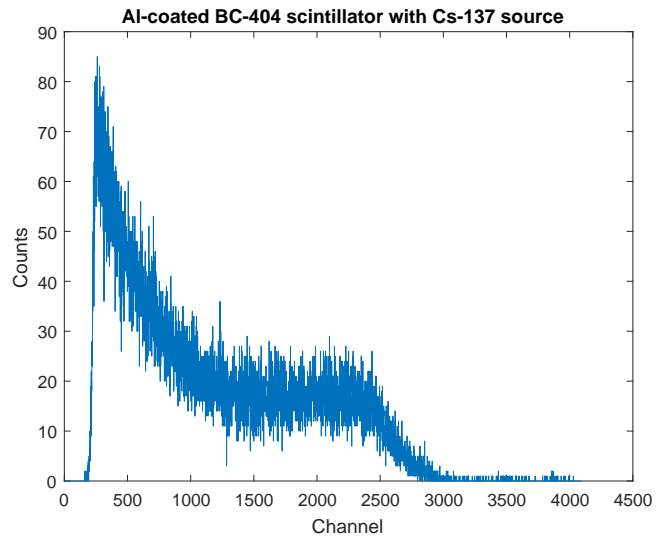
3.3 Aluminium coated plastic scintillator

The black surface is causing some of the scintillation light to not reach the PMT as seen above. To reduce this effect, a BC-404 scintillator is coated with aluminium to create a reflective layer instead of an absorbing one.

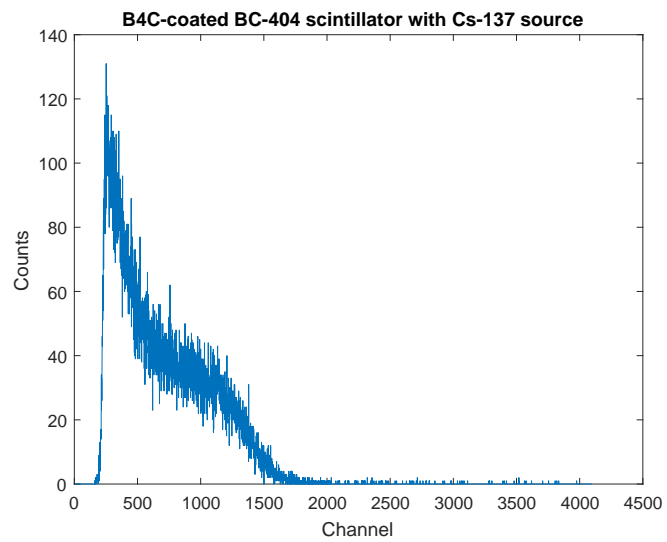
It would then be possible to (though it is not tried in this project) coat a plastic scintillator first with aluminium and then with boron carbide on top of this. The aluminium would have to be thin, to not stop the alpha particles from the B_4C layer to much and thus, if not stop them all together, worsen the energy resolution.

The response of BC-404 scintillators coated with Al and B_4C respectively mounted on a PMT is investigated using a ^{137}Cs gamma radiation source. The obtained energy histograms are shown in Figure 3.4. Figure 3.4a shows the energy histogram of an aluminium coated scintillator. The Compton edge from the 661 keV photon is at about channel 2800, which is much higher than for the B_4C coated scintillator for which it lays at about channel 1600, 57 % of the value obtained for the aluminium coated. This suggests that a scintillator with a thin aluminium coating under a boron carbide coating may give a more distinctive signal than one with only a B_4C coating.

A non-coated BC-404 scintillator was also tested as a reference. The result of this is seen in Figure 3.5. The Compton edge for this scintillator is much higher than it is for the Al-coated one. Either something happens with the scintillator plastic in the coating process that makes it lose some of its scintillation properties, or the aluminium coating does not provide a good mirror for the scintillation light.



(a) Al-coated scintillator



(b) B₄C-coated scintillator

Figure 3.4: Energy histograms of BC-404 scintillators coated with aluminium and boron carbide when a ¹³⁷Cs source is used.

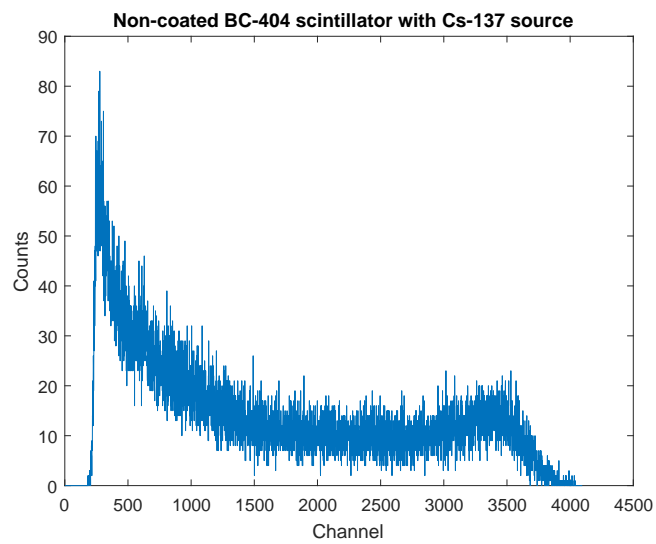


Figure 3.5: Energy histogram of a non-coated BC-404 scintillator radiated by gamma rays from a ^{137}Cs source.

3.4 Potentially damaged surface layer of plastic under boron coating

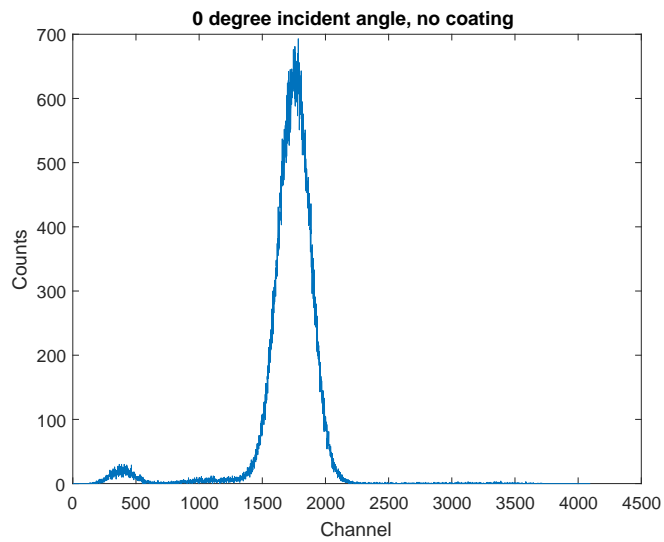
There is a possibility that the plastic scintillators that has gone through the process of being coated with boron carbide have been somewhat damaged. The damage would in that case most likely be in the region of the plastic that is closest to the applied boron carbide layer.

To test this, scintillators with and without boron carbide coating have been mounted in the experimental chamber for the LIBAF μ -beam accelerator where it is radiated by monoenergetic protons. The scintillators has been mounted both so that the proton beam hits the scintillator at a right angle to the surface (referred to as 0°) and at a 45° angle. The protons will then travel different distances in the topmost layer of plastic which would result in a different amount of energy being deposited in the scintillator, and a different light output if the properties of this layer has been affected. The energy loss of the proton in the boron carbide layer would also have to be accounted for, since the protons would travel different distances also in this layer with different angles of entry. The protons hitting the scintillators had an energy of 2.5 MeV.

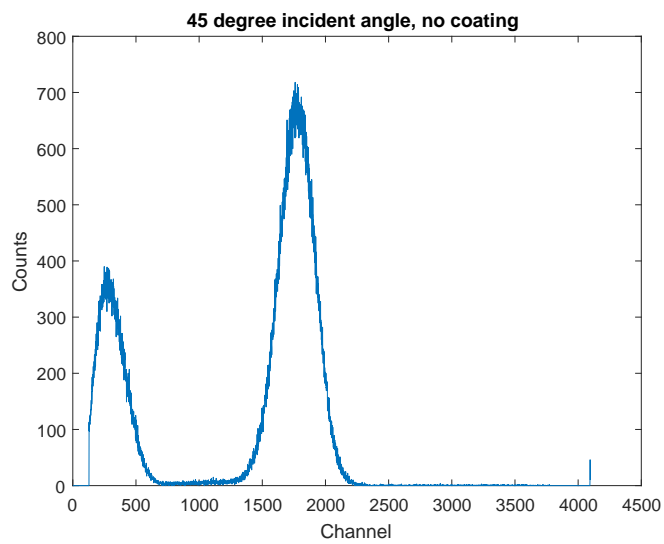
The scintillators used in this case was a non-coated BC-404 plastic scintillator and a boron carbide coated BC-404 one with 1 μm thick layer of boron carbide. To read out the signals an APD-S8664-SPC1010 (2CH) LAAPD (described further in Chapter 4) was used. This in turn was coupled to an AMPTEK A250CF coolFET charge sensitive preamplifier. The signals were then shaped in an amplifier and collected by an ADC. The gate to the ADC was created in a Single Channel Analyser (SCA). This was done by feeding the SCA a bipolar signal (both a positive and a negative lobe following one another) from the amplifier, and it created a gate at the point the bipolar signal crossed the zero level. This occurs at the same time relative to the pulses beginning independent of pulse height.

For the case of the non-coated scintillator, the results are seen in Figure 3.6. In Figure 3.6a the protons collided with the scintillator head on, while in Figure 3.6b the beam had an incidence angle of 45° .

In the figures two peaks are seen. The one higher in energy represents the energy deposited by the protons, while the lower one comes from noise. The proton peak is in the same place both in Figure 3.6a and 3.6b. Thus the proton energy deposition in the scintillator is the same regardless of angle of incidence. Something that can be seen in Figure 3.6 is that the noise level is different between the measurements. Noise was an issue during the experiment and it is not surprising if the magnitude of the noise would change. It is also possible that the lower discriminator level on the SCA used to generate the gate to the ADC was changed slightly.



(a) 0° incident angle



(b) 45° incident angle

Figure 3.6: Non-coated BC-404 scintillator radiated by a 2.5 MeV proton beam

Figure 3.7 shows the results for the measurements on the coated diode. Also here the angle of incidence seems to be unimportant. What is remarkable is the movement downwards of the peaks in the spectrum compared to what is seen in Figure 3.6. The peak position has changed to channel 800 from 1800, a reduction by more than half. This makes the peak originating from the proton energy deposition only just discernible from the peak originating from noise.

The energy deposited by the proton in the boron carbide is not released as scintillation light and thus will not be detected. This energy can be calculated by Equation 2.7, to see how much effect this energy loss has. The stopping power is calculated in the SRIM software to be $27 \text{ keV}/\mu\text{m}$ of 2.5 MeV protons in B_4C . This is a small loss of energy and thus the stopping power is assumed to be constant through the layer. The B_4C layer is $1 \mu\text{m}$ thick, and thus the proton energy loss is 27 keV.

A difference of 27 keV will only move the peak about $\frac{1800}{2500}27 = 19$ channels which is hardly visible. The change from a 0 degree incidence angle to a 45 degree one will have an even smaller effect on the peak position. Since no change is observed in the position of the peak between Figure 3.7a and 3.7b, it is also concluded that it is not a damaged non-scintillating layer of the scintillator that is causing the loss of energy.

The only major difference left between the scintillators of Figures 3.6 and 3.7 is the black surface that the B_4C coating brings. In Section 3.2.1 this effect is tested using a gamma radiation source, scintillators mounted on a PMT, and the surface blacked by tape. There it was found that the black surface caused a loss of about 25 % of the scintillation light. In this measurement it would seem that more than half of the scintillation light is lost. The B_4C coating is deposited onto the scintillator surface much tighter than the tape used in Section 3.2.1, which might be an important factor in how much light is absorbed. In this case the scintillation light may not really have to exit the scintillator before the light could be absorbed, but could be absorbed directly in the connected surface junction.

To investigate the potential presence of a non-scintillating layer under the coating one could use lower energy protons. Those would lose a larger part of their energy in the would be dead layer which would give a larger effect to the change in peak position when the angle of the incoming particles is changed. However, considering that the peaks from the protons in Figure 3.7 lies very close to the noise level (the lower peaks in the energy spectrum), the energy 2.5 MeV is about as low as one can get. Using a lower proton energy it would not be possible to discern the signals from the protons from the noise.

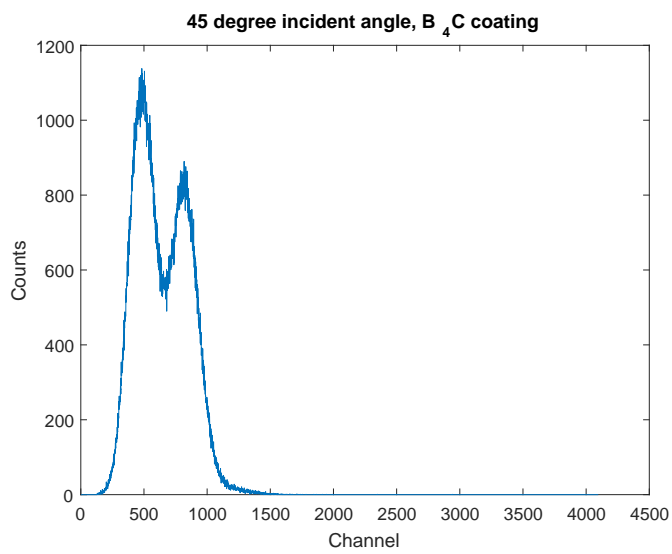
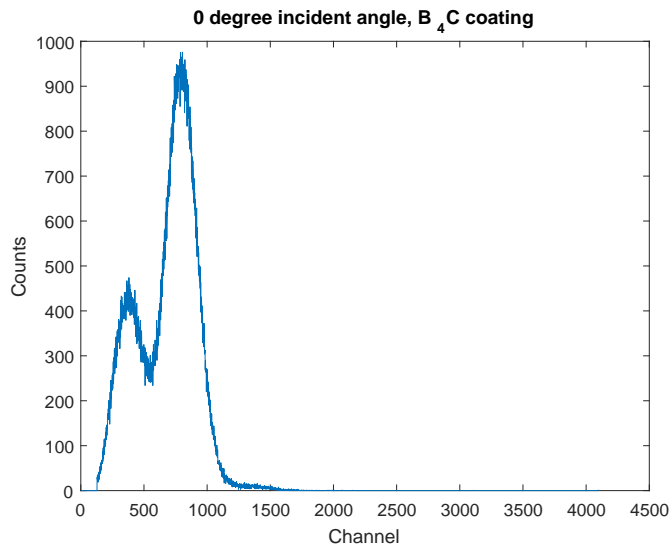


Figure 3.7: Coated BC-404 scintillator radiated by a 2.5 MeV proton beam

Chapter 4

Photomultiplier Tubes or Avalanche Photo Diodes

There are a number of ways to read out signals from a scintillator, of which two examples are the PMT and the APD. There are both advantages and disadvantages with the two systems and some prioritising has to be made.

An apparent difference between the systems are the size. The PMT is much larger than the APD, which would make a system that uses APDs easier to handle. The APDs also in general operate at a smaller bias than the PMTs do which could be beneficial. Some of the other differences are illuminated in this chapter.

4.1 The APDs

The APDs used for these tests are Large Area Avalanche Photo Diodes (LAAPD) developed by the R³B collaboration along with Hamamatsu, called APD-S8664-SPC1010 (2CH) [29]. It is two Hamamatsu S8664-1010 Si APDs combined into the same ceramic casing [29]. Three specimen of these APDs are seen in Figure 4.1.

They have a large active area of $2 \times 100 \text{ mm}^2$ which allows it to gather much of the scintillation light even though no light guide was used. A large area diode also has a large terminal capacitance, and one Hamamatsu S8664-1010 Si APD has a terminal capacitance of 270 pF [30], and the capacitance of these APDs would be the double. This can cause some problem with noise if a preamplifier is used that is not matched to a large terminal capacitance.

The spectral response of a Hamamatsu S8664-1010 Si APD is shown in Figure 4.2 from the datasheet [30]. It is the higher graph of the two in the figure that represents the response of the APD in question. There it is seen that the current out per incoming photon power drops for wavelengths under 500 nm, and is thus not optimal for wavelengths of about 420 nm which is the case for the plastic

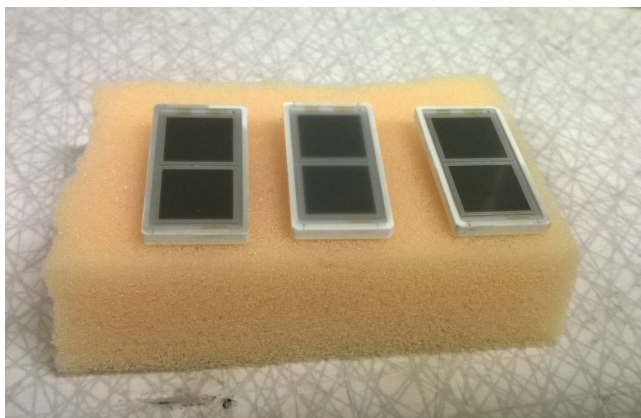


Figure 4.1: Three APD-S8664-SPC1010 (2CH) LAAPDs

■ Spectral response

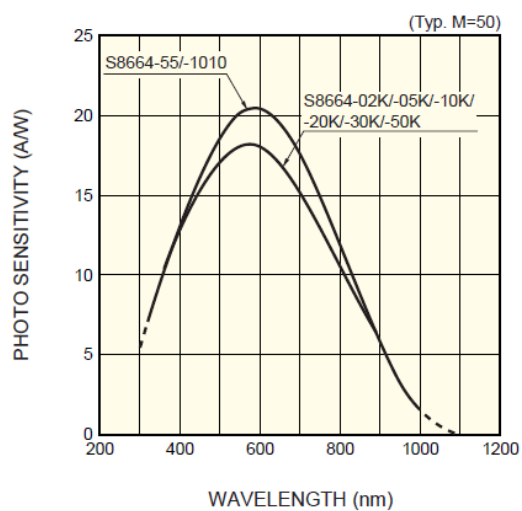


Figure 4.2: The spectral response of a S8664-1010 APD as a function of incoming light wavelength. Figure from Hamamatsu S8664-1010 Si APD datasheet [30].

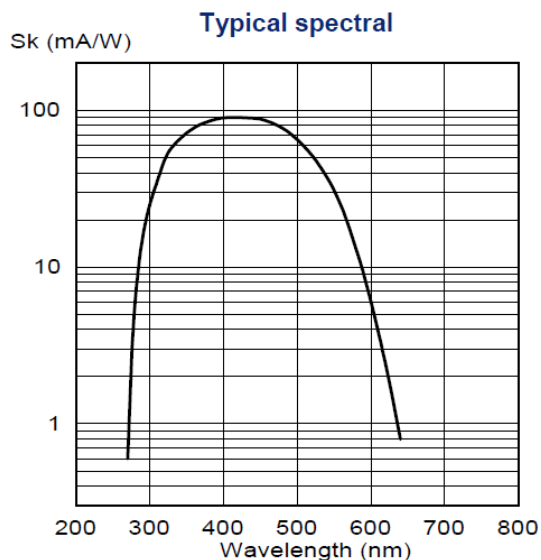


Figure 4.3: The spectral response of a the RTC XP 2262 B PMTs as a function of wavelength. Figure from the datasheet [31]. Notice the logarithmic scale on the ordinate axis.

scintillators. It is better adapted for a CsI(Tl) crystal for instance, which has a maximum emission wavelength of 550 nm.

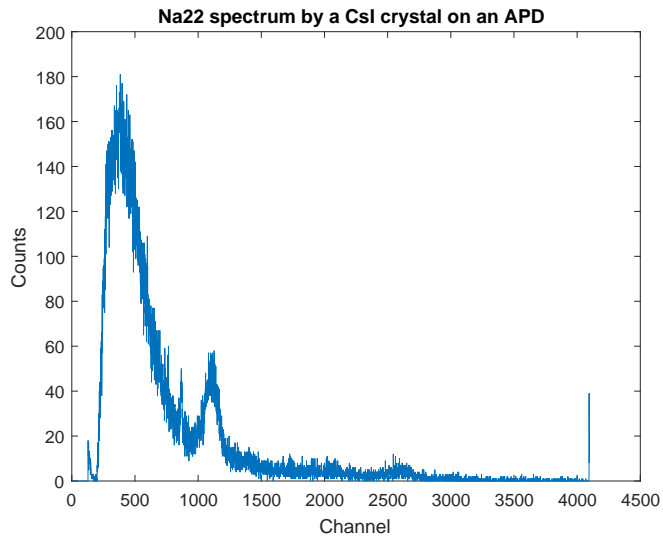
4.2 The PMTs

The PMTs utilised in the experiments are of the make RTC (now Photonis) XP 2262 B [31]. Figure 4.3 from [31] shows typical values of the spectral response for the PMT. The response is largest for incoming light with wavelengths about 400 nm, which is the case for the plastic scintillators. It has a slightly worse response for longer wavelengths were the APDs had its peak.

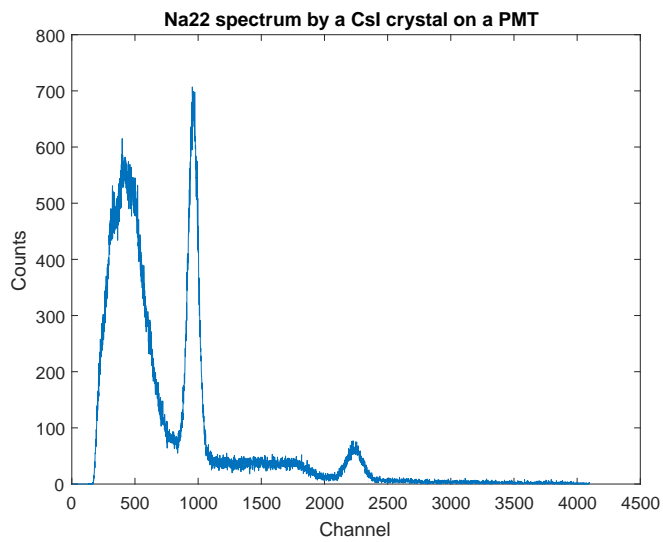
4.3 Resolution

Energy spectra of ^{22}Na has been taken with a CsI(Tl) crystal mounted on the APD and the PMT in turns to be able to make comparisons between the two. Figure 4.4 shows the energy spectra obtained, Figure 4.4a with the APD used and Figure 4.4b with the PMT. Both spectra were acquired during a time period of about one hour. In both figures the 511 keV peak lies close to channel 1000.

The resolution of the PMT and the APD based on the 511 keV peak for each seen in Figure 4.4 is calculated as the FWHM value divided by the channel number of the peak value. For the APD this is $\frac{135}{1110} = 0.12$ and for the PMT $\frac{105}{960} = 0.11$.



(a) APD



(b) PMT

Figure 4.4: Na22 spectra taken by a CsI(Tl) scintillator mounted on an APD and a PMT respectively

The amount of data collected is much larger for the PMT than for the APD. For instance the number of counts per minute in the 511 keV peak is about 100 for the APD and 900 for the PMT. The source was put in close proximity to the CsI(Tl) crystal in both measurements, so this is not the source of the discrepancy.

There is a difference in effective area of the PMT and the APD. The APD area is 2 cm², while the PMT window area is about 15 cm² and it covers the whole of the CsI(Tl) crystal surface which is about 6 cm². Thus only a third of the surface of the CsI(Tl) is covered when an APD is used which makes it possible for more light to be lost when this is used instead of a PMT.

One would in that case expect the resolution of the APD to be a lot worse than that of the PMT if many more photons are lost due to the bad area coverage by the APD. However, the spectral response presented in Figures 4.2 and 4.3 shows that the APD is more suited to pick up the scintillation light from a CsI(Tl) crystal than the PMT is. Thus the APD can convert a larger fraction of the photons that actually hit its surface into current than the PMT can. This compensates for the fact that more photons are lost because of the smallness of the APD area.

The question of the count rate difference in the photoabsorption peak still remains. There is a possibility that it has something to do with the geometry of the system, originating in the fact that the APD does not cover the full crystal surface. This may introduce some effects which could be helped with the use of a light guide used to channel all the light from the scintillator to the APD.

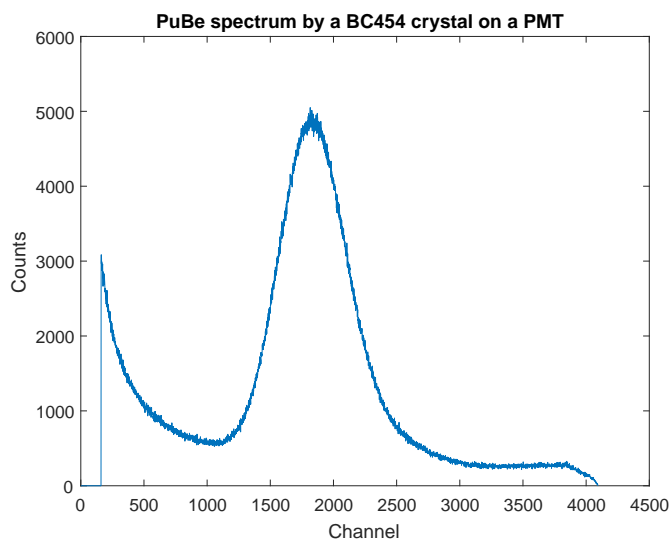
4.4 Neutron measurements with APD

Signals from the residual alpha particle after the boron-10 reaction with neutrons has proven difficult to detect using an APD. Both for boron carbide coated plastic scintillators (described in Chapter 3) and a Saint-Gobain boron loaded plastic scintillator BC-454.

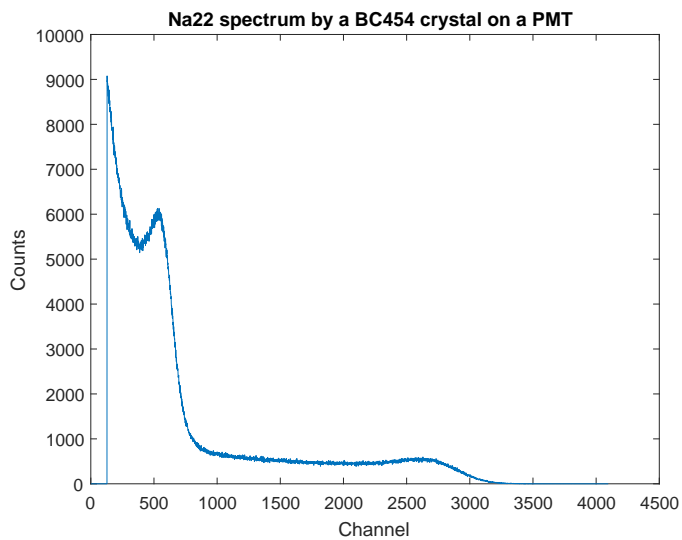
The alpha particle signal seems to be hidden under the noise when an APD is used, but not when a PMT is. An approximate calculation of the quenching of alpha particle response in the scintillator compared to photon response can be made by comparing the energy spectrum arising from neutrons taken using the BC-454 scintillator on a PMT, with an energy spectrum from gamma rays by the same means of acquisition.

Figure 4.5 shows energy spectra where the energy depositing particles are alphas and photons in Figures 4.5a and 4.5b respectively. The peak in Figure 4.5a originates mainly from alpha particles with energy 1.47 MeV, and the gain of the PMT was about $2 \cdot 10^8$, where the gain value comes from a typical gain curve in the PMT datasheet [31]. The signal from the lithium ions contribute some also, but they are quenched even more than the alphas so the most part of the signal will be induced by the alpha particles. The peak is seen at channel 1835.

The edge at channel 830 in Figure 4.5b originates from the Compton edge of 511 keV gamma photons from the ²²Na source. The Compton edge lies at an



(a) Alpha particle induced signal. PMT gain $2 \cdot 10^8$



(b) Photon induced signal. PMT gain $2 \cdot 10^7$

Figure 4.5: Energy spectra where the energy deposition in the scintillator comes from alpha particles and photons respectively. The scintillator is a boron loaded plastic BC-454. The alpha particle release is induced by a PuBe source, and the photon signals come from a ^{22}Na source. The signals from the PMTs were analysed with a QDC unit.

energy of 341 keV as calculated by Equation 2.5. The PMT was operated at a gain of approximately $2 \cdot 10^7$.

Assuming a linear behaviour of the system the energy per channel per PMT gain is calculated for alphas as $4 \cdot 10^{-12}$ MeV/ch/gain and photons as $2 \cdot 10^{-11}$ MeV/ch/gain. Thus there is a factor 20 of quenching for alpha particles compared to gammas.

A quenching factor of 20 for alpha energies around 1.5 MeV for some other plastics is also what is found by a Tretyak in [32]. The quenching factor there is defined as the light yield of an alpha particle in relation to that of an electron, and not a gamma. However, in the photon interactions with matter an electron is knocked out from the atom and deposits its energy in the scintillator, which makes the numbers relevant. All plastics that are described there has a maximal quenching of the light yield from alpha particles around this energy, which suggests that this may also be the case for PVT which is the plastic material that the scintillators here are made up of.

In [33] it is concluded that an APD (or at least the APD used there, an RMD S0223 APD) has a worse signal to noise ratio than a PMT for small signals of light in the visible region. The scintillation light of the plastics is in the visible region, with a wavelength of about 400 nm as written in Table 2.1. These factors described, and not forgetting the slight mismatch between the APDs and the plastics in terms of spectral response, suggests that there may be an inherent difficulty of reading out the alpha signals on the APDs.

To illustrate the problem an energy spectrum taken by the BC-454 scintillator is shown in Figure 4.6. The BC-454 is mounted on an APD and a ^{137}Cs gamma ray source is present. The Compton edge of the 661 keV gamma signal lays at about channel 1250 in the spectrum which would correspond to an energy of 477 keV according to Equation 2.5. The noise in the system reaches up to around channel 360. The signal from a 1470 keV alpha particle would in this case lay at a channel number of $1250 \frac{1470}{477 \cdot 20} = 193$ if a quenching factor of 20 is assumed for an alpha signal compared to a gamma signal. This is far down in the noise, and the signal would not be visible.

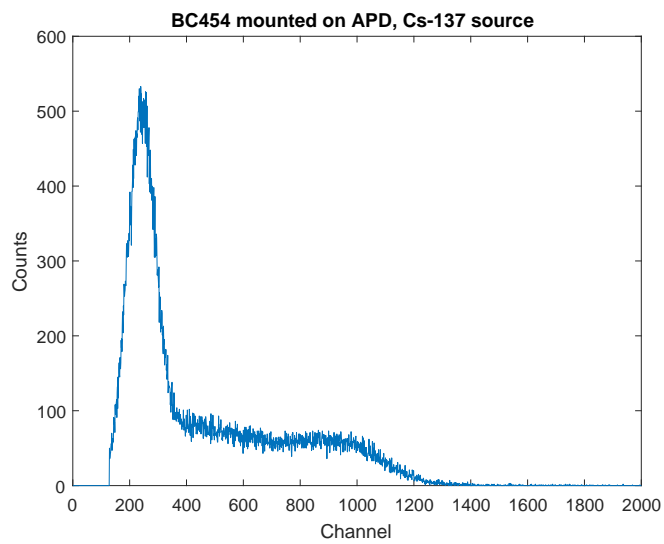


Figure 4.6: Energy spectrum of a ^{137}Cs source taken by a BC-454 boron loaded plastic scintillator mounted on an APD

Chapter 5

Boron loaded plastic together with an inorganic crystal scintillator

Two different particle types are supposed to be detected; the alpha particle and lithium ion originating from the boron neutron reaction described in Equation 2.1, and the gamma photon emitted by the lithium ion relaxing to its ground state. The purpose of having two different scintillators is thus to detect the charged particles in one specialised for this purpose and the photon in another specialised for this. Being able to apply a coincidence condition on these two separate particle detections will reduce the background and give a more specific neutron signal.

A photomultiplier tube is a rather large device. The ones used here are in themselves well over a decimetre long (there are smaller ones however). To save space and to get a more compact end system, the two scintillators are mounted on the same PMT, and a pulse shape discrimination (PSD) technique is used to separate the signals from the different scintillators.

This looks as shown in Figure 5.1. Here a CsI(Tl) crystal is mounted on a BC-454 plastic scintillator which in turn is mounted on a PMT. The scintillation light from the CsI(Tl) must then travel through the BC-454 before it reaches the PMT window.

APDs are much more space efficient than PMTs, and would be a nice alternative to use. In Chapter 4 was concluded that the signal from the alpha particle released in the boron capture reaction was not visible when using an APD (at least with the noise level present there), thus only the PMT alternative is utilised here.

The two scintillators simultaneously mounted are a boron loaded Saint-Gobain plastic scintillator BC-454 [13] along with an inorganic crystal scintillator. The inorganic crystals tested are CsI(Tl) and a Saint-Gobain P420 [34]. Additional information about these scintillators is found for the BC-454 in Table 2.1 and in

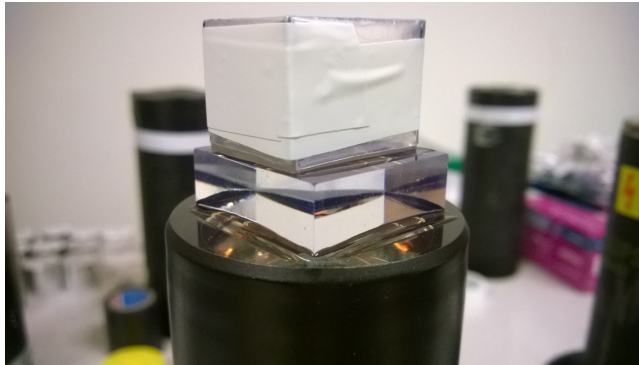


Figure 5.1: A PMT with the BC-454 scintillator mounted on it, and on top of the BC-454 a CsI(Tl) crystal is mounted

the data sheet [13], and about the inorganic scintillators in Table 2.2. Relevant features are brought up along the way as this chapter progresses.

It is the boron loaded BC-454 scintillator that will be used in these measurements and not a boron coated one. This because the neutron induced signals in the BC-454 is much more clearly visible than the signals originating from neutrons in a coated plastic scintillator as was found by Bodahl [27].

In this chapter the process of going from separate scintillators, each on its own PMT, to having both scintillators on the same PMT will be described, and the neutron detection ability of the systems will be discussed.

5.1 CsI(Tl) crystal measurements

The measurements conducted using a CsI(Tl) crystal scintillator along with the BC-454 one will be presented in this section. The measurements where the scintillators are mounted on the same PMT will be presented in Section 5.3.2.

5.1.1 The CsI(Tl) crystals

Caesium iodide crystals are slightly hygroscopic, which means that they are a bit sensitive to humidity. After some time the crystal material therefore becomes slightly matt and opaque. This was to some extent the case with the crystals used here. After some polishing of the surfaces the crystals became clearer and were deemed fit for use.

There were two crystals that were used in measurements, one large and one smaller. The big one was $4.0\text{ cm} \times 4.0\text{ cm} \times 10.0\text{ cm}$ and is seen in Figure 5.2. It had reflecting material wrapped around it on the sides so that as little scintillation light as possible is lost.

The smaller CsI(Tl) scintillator that is used can be seen in Figure 5.1 as the top-most scintillator. Also this is covered with reflecting material which in this case



Figure 5.2: The larger of the two CsI(Tl) scintillators used

is held onto place with white tape as seen in the photograph. The dimensions of this one is $2.0 \text{ cm} \times 2.1 \text{ cm} \times 2.8 \text{ cm}$.

5.1.2 Coincidence measurements with CsI(Tl) and BC-454

A schematic view of the measurement set-up is shown in Figure 5.3. Here the large CsI(Tl) crystal is used, and is put closely to the BC-454 plastic to catch as many of the 478 keV photons released as possible. The reason that the coincidence unit is used in this set-up and the CFD signal is not directly sent to the gate generator, is that the coincidence unit used has a veto signal input. This signal is fed from busy signals from the ADC and QDC units and the data acquisition system in general, which means that the coincidence unit will not send out a gate generating pulse when the system says that it is already occupied.

In this set-up the QDC, ADC and TDC units are gated and triggered by a signal from the BC-454 scintillator only. Thus it is not only coincident signals that is collected, but the BC-454 signals and whichever signal that happens to be there from the CsI(Tl) scintillator.

The coincidence requirement is applied later based on the collected TDC signals. If one applies three conditions on the collected data; that there should be signals in the QDC (or ADC, but here the QDC signal is used) and TDC units from both scintillators, and that the signals to the TDC should have been collected at specific points in time relative to the TDC trigger signal from the gate generator, one may extract the coincident pulses in the scintillators.

Plotted as a histogram, the time difference between the BC-454 and CsI(Tl) discriminator signals are seen in Figure 5.4. The peak in the spectrum represents the events with the most frequent time difference of the signals from the respective scintillators close enough in time to one another to appear in the same TDC window. These are interpreted to be originating from the true coincident signals.

There has been some fluctuations and drifts in energy in the measurement sys-

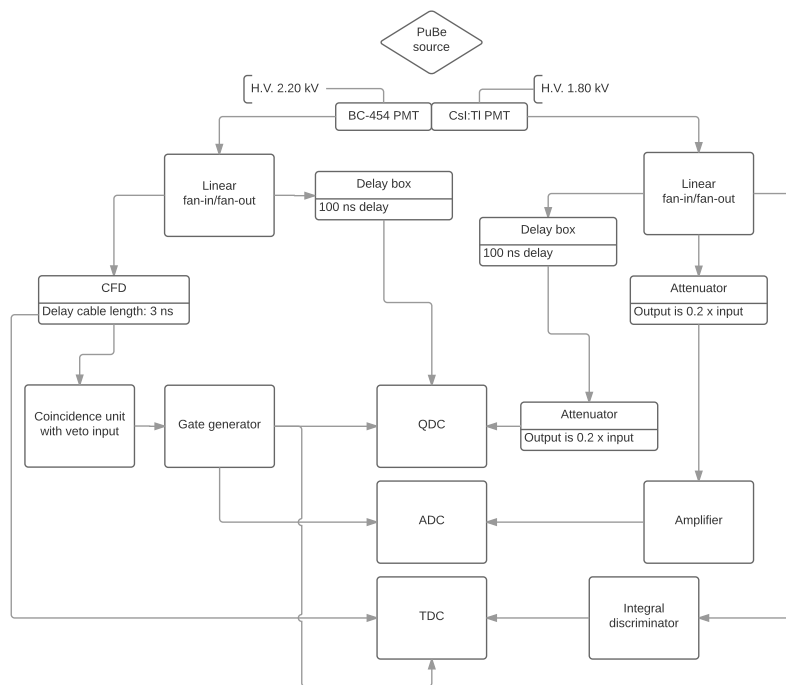


Figure 5.3: The coupling scheme of the coincidence measurement with CsI(Tl) and BC-454 in a schematic fashion

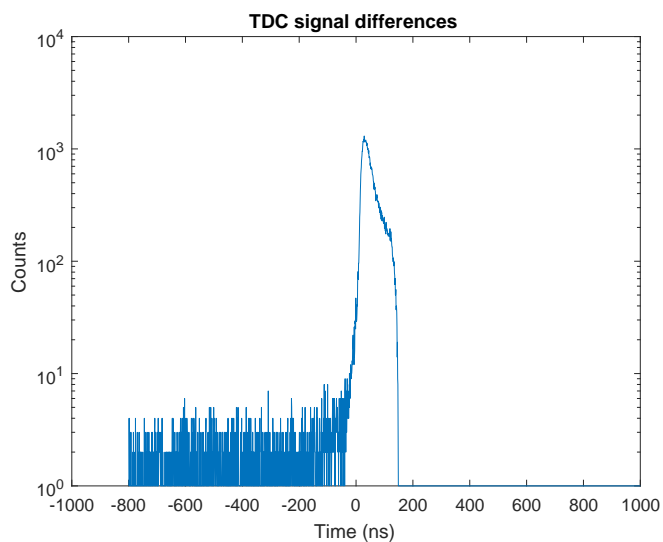


Figure 5.4: Time difference of the signals to the TDC unit generated by the CsI(Tl) and BC-454 scintillator pulses

tem. On some occasions energy peaks has been observed to drift, and seemingly change energy which demands some caution from the user. The result of this is that even if the system was stable during a run, an exact energy calibration might be difficult to preform.

Such is the case in the coincidence measurements with CsI(Tl) and BC-454. An energy calibration was not preformed immediately in connection to the measurement, and the calibration run preformed would put the 478 keV peak of interest at a slightly different energy than optimal. Therefore non-calibrated channel numbers are used in this section.

The signals which has created the time peak in Figure 5.4 are plotted as energy histograms in Figure 5.5 and comes from the CsI(Tl) and the BC-454 scintillators respectively. Figure 5.5a shows a clean spectrum with a photoabsorption peak just above channel 3000 from the 478 keV photons, and lower in energy are signals which likely originates from the Compton scattered photons of the same energy. This is the energy spectrum in the QDC unit, not the ADC which would have been possible to use also. The BC-454 energy spectrum in Figure 5.5b has very little background around the peak originating from the alpha particle and lithium ion.

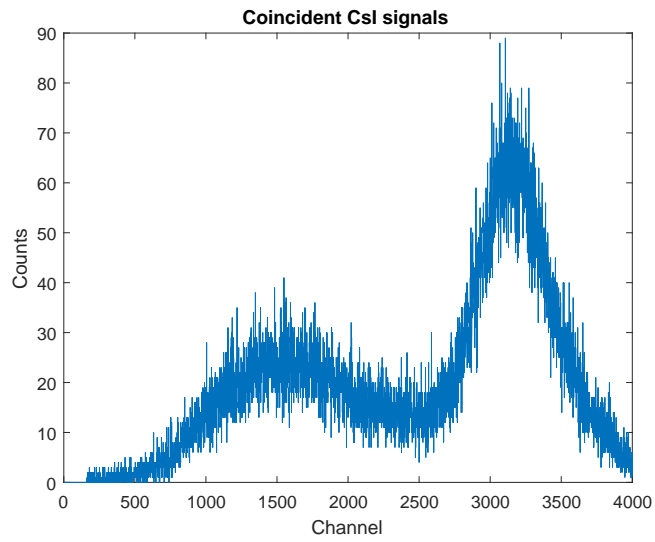
These energy spectra can be compared to the ones taken by the QCD before any conditions were applied. These are shown in Figure 5.6. Regarding the case of the CsI(Tl) in Figure 5.6a, the peak from the 478 keV lithium de-excitation gamma is of similar height but there are a lot of low energy noise also. This noise is removed with the timing conditions applied which is highly desirable.

The energy peak in the boron loaded BC-454 plastic is much bigger in Figure 5.6b than in Figure 5.5b as could be expected. The amount of signals in the peak that disappears when the coincidence criteria are applied are interesting in terms of the relation between added certainty that the event in the peak is actually induced by a neutron, and the decreased efficiency for the number of events discarded because the photon from the lithium ion missed the CsI(Tl) scintillator.

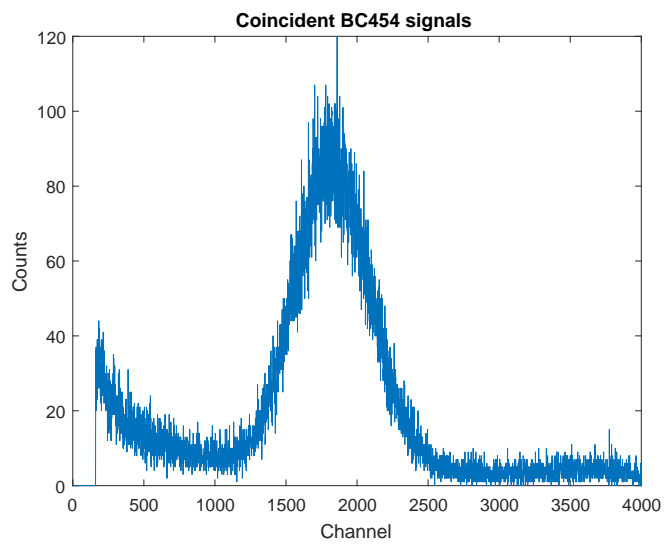
The number of events in the peak in Figure 5.6b is 3335849 if the peak is defined to lay between channels 1263 and 2378. For the same interval in Figure 5.5b the number of counts are 56786. Thus only 1.7 % of the original counts are left. It would seem that the coincidence condition in this case comes at a high price.

One can with some benefit make a two dimensional energy plot with the BC-454 channels on one axis and the CsI(Tl) on the other. This is done in Figure 5.7. In this figure the energy deposited in the CsI(Tl) crystal is presented on the abscissa and the energy of the coincident pulse from the BC-454 scintillator is on the ordinate in terms of channels/10. The color surface of the figure represents the number of counts in each pixel (i.e. a 2D histogram).

The circular peak around coordinates (315,183) in Figure 5.7 corresponds to the coincidental events of photoabsorption of a 478 keV photon in the CsI(Tl) crystal with an alpha particle and Li-ion from the boron-neutron reaction in the BC-454 scintillator. The number of counts in this peak would correspond to the number of fully defined neutron capture events. Between channels 1260 and 2370 on the ordinate, and between 2700 and 3650 on the abscissa in Figure 5.7

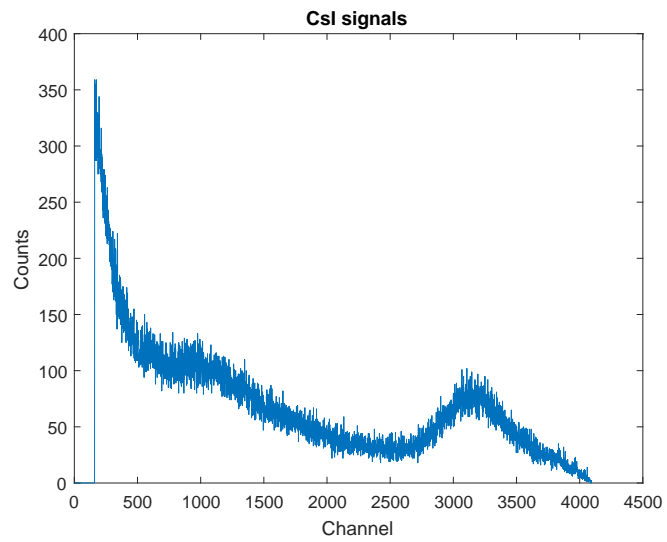


(a) The signals from the CsI(Tl) scintillator which has originated coincidentally with signals in the BC-454 scintillator

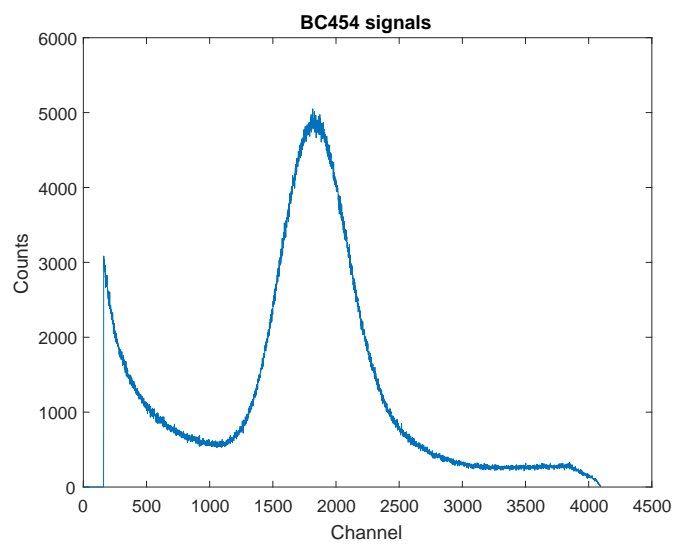


(b) The signals from the BC-454 scintillator which has originated coincidentally with signals in the CsI(Tl) scintillator

Figure 5.5: Coincidental energy spectra



(a) $CsI(Tl)$



(b) $BC-454$

Figure 5.6: Energy spectra obtained by the QDC as displayed in Figure 5.3 with no further conditions on coincidentality

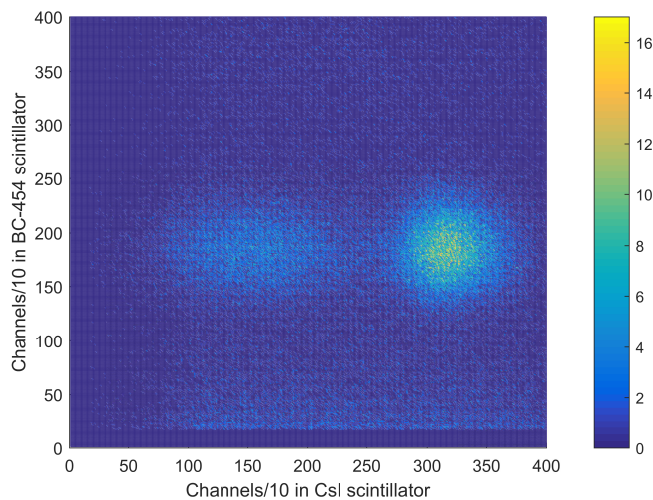


Figure 5.7: 2D energy plot of the coincident CsI(Tl) and BC-454 signals against each other

on a square region, the number of events are 32916. This is 1 % of the counts in the unrestricted peak in Figure 5.6b.

5.2 PreLude 420 crystal measurements

PreLude 420 ($\text{Lu}_{1.8}\text{Y}_{0.2}\text{SiO}_5:\text{Ce}$) was one of the candidate crystals for measuring the 0.48 MeV gamma ray released from the excited ${}^7\text{Li}$ nucleus left after the ${}^{10}\text{B}$ neutron capture reaction. First some information about the crystal used is presented, then a coincidence neutron measurement with a BC-454 scintillator like the one for the CsI(Tl) crystal.

5.2.1 The P420 crystal

The P420 crystal used here was cylindrical in shape with chamfered edges. One of the edges of the cylinder was polished while the rest of the crystal surface was a bit ragged and cloudy in appearance. The cylinder diameter is 25.52 mm and the height 35.17 mm, thus a crystal volume of $17.99 \text{ cm}^3 \approx 18 \text{ cm}^3$.

There is a large intrinsic activity of the P420 crystal. It amounts to 39 counts per second per gram [34]. With a density of 7.1 g/cm^3 [34] this translates to a registered activity of 5 kHz. The activity originates from the radioactive isotope ${}^{176}\text{Lu}$ that can be found in the crystal [34]. ${}^{176}\text{Lu}$ decays by β^- -decay to an excited state in ${}^{176}\text{Hf}$, 597 keV above the ground state 99.66 % of the time [34]. The excited Hf nucleus decays by three gamma emissions with energies 307 keV, 202 keV and 88 keV [34]. The resulting background spectrum originating from this activity can be seen in Figure 5.8. The sort of staircase shape of the

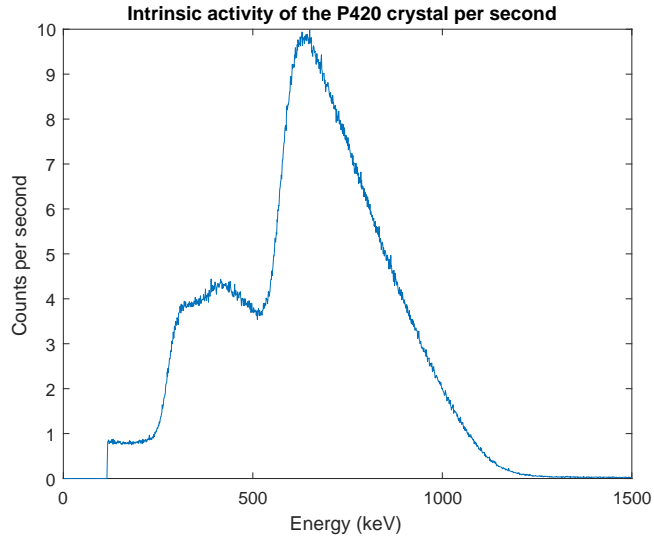


Figure 5.8: The intrinsic activity per second of the P420 crystal used

energy spectrum is produced from when one or more of the photons from the de-excitation cascade escapes from the crystal without being absorbed.

The 478 keV photon which is interesting in this application is thus covered by the intrinsic background from the P420 crystal. This presents some added difficulty of course. Since the signals are quite short in time, the decay time of the crystal is only 41 ns, most of the time there are no signals in the system. Using a coincidence criteria between a signal in the BC-454 boron plastic scintillator and the P420 crystal the 478 keV photon signal might still be visible over the background.

5.2.2 Coincidence measurements with P420 and BC-454

In this measurement a hardware coincidence condition was enforced on the signal before sent to the data acquisition system, instead of using a time difference criteria based on the TDC signals. A schematic of the experimental set-up is presented in Figure 5.9.

If the CFD signals to the coincidence unit overlap, the coincidence unit will send out a gate signal to the QDC during which the delayed signals to the QDC are integrated. They are both fitted so that they arrive well within the gate if they are coincident. The coincidence unit will also send a pulse to the gate generator unit to there create a longer gate to the ADC, and a trigger pulse to the TDC. The TDC will also receive the CFD signals so a time structure of when which pulse arrives can be seen if wanted. The QDC signals will be used in this case, and the ADC (and TDC) signals will be left untouched.

The energy spectrum of the gamma radiation detected by the P420 scintillator according to the set-up in Figure 5.9 is presented in Figure 5.10. The scintillator was energy calibrated using a ^{22}Na source. The peak from the 478 keV

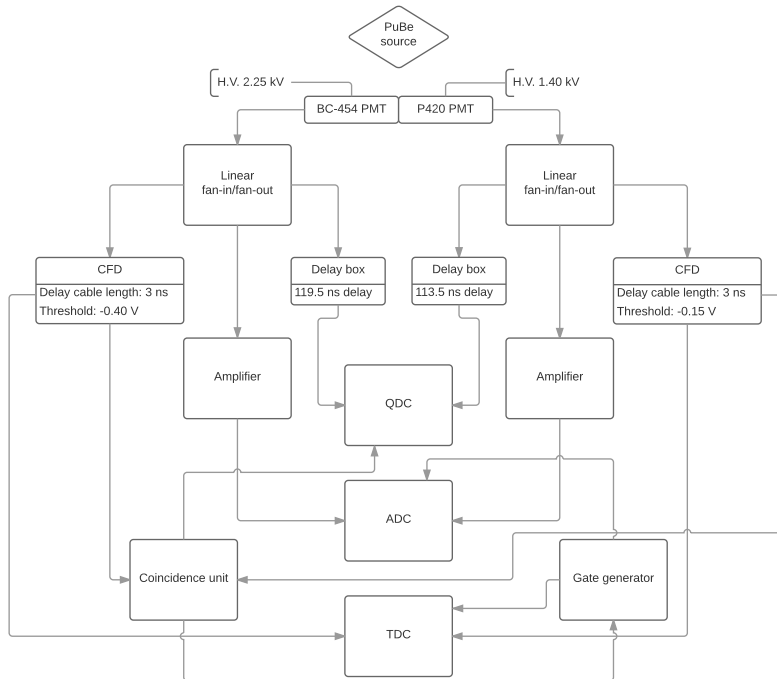


Figure 5.9: The coupling scheme of the P420 BC-454 coincidence measurement in a schematic fashion

radiation is seen above the background of intrinsic radiation of the crystal with the coincidence condition applied.

Figure 5.11 shows the energy histogram obtained by the BC-454 plastic scintillator in the set-up described in Figure 5.9. The peak seen at just above channel 1000 originates from the boron neutron reaction.

Combining the energy histograms from Figures 5.10 and 5.11 by plotting the coincident energies against each other the 2D histogram in Figure 5.12 is created. The neutron events are grouped together in an oval region at coordinates (48,110) in the figure.

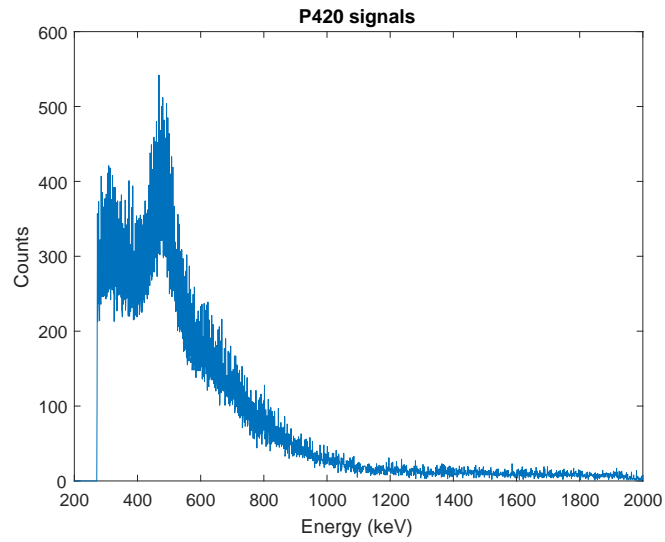


Figure 5.10: The P420 signals coincident with a signal from the BC-454 scintillator. Energy calibrated using a ^{22}Na source.

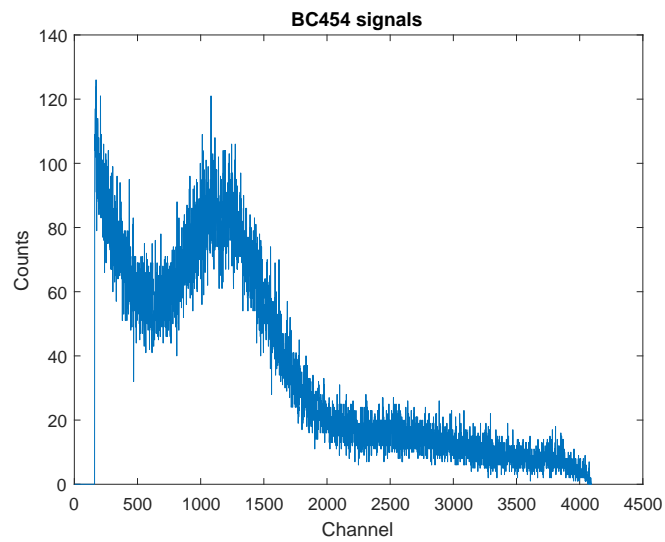


Figure 5.11: The signals in the BC-454 scintillator acquired coincidentally with a signal in the P420 scintillator.

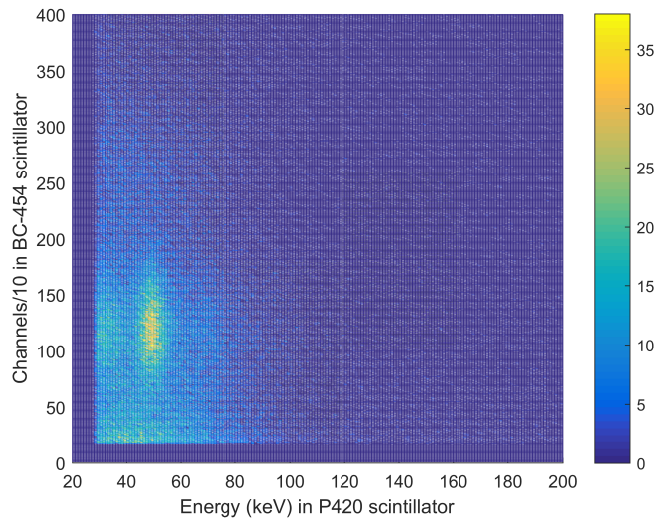


Figure 5.12: The 2D energy histogram over the coincident energy depositions in Figures 5.10 and 5.11

5.3 Scintillators mounted on the same PMT

To still be able to read out the signals from the scintillators even if they are collected by the same PMT, some sort of Pulse Shape Discrimination (PSD) needs to be utilised. This is done as follows.

5.3.1 Pulse shape discrimination between scintillators mounted on the same PMT

Pulse shape discrimination is used mainly for sorting out signals originating from one specific type of particle inside a detector. For instance one may have a detector material sensitive for both neutrons and photons, and only want to detect the neutron signal. Since the particles interact with and transfer energy to matter in different ways, it follows that the material also subsequently de-excite in different ways. For instance the time constants of the scintillator decay may differ with impinging particle, which means that the pulse shape out of a detector will be different depending on which type of particle has deposited energy in it.

There are different ways one may differentiate between pulse shapes. Some schemes are zero crossing PSD, rise-time discrimination and the charge comparison method. Here the charge comparison method will be utilised.

The charge comparison method is based on the different decay times of the scintillator that comes with different particles. For instance one can integrate the beginning of the pulse and the whole of the pulse separately and make a ratio of these integrals. Different decay times of the pulses will mean different



Figure 5.13: Pulses from one PMT containing contributions from both a BC-454 and a CsI(Tl) scintillator

ratios of the integrals for certain particles, and one can thus extract the signals from the desired particle type.

For the application described here, the PSD is not for discriminating between pulses that originate by different particles in the same scintillator, but different particles in different scintillators. The pulse shapes need not resemble each other at all in this case. This makes the considerations needed to be taken into account different from what is customary.

However, the decay time of the BC-454 scintillator is short compared to the inorganic crystals. Summing a pulse from the two scintillators will mean that the beginning of the pulse will contain a large contribution from the BC-454 scintillator, and after this signal has faded the only contribution will be from the inorganic crystal. If both scintillators leave a contribution simultaneously, the ratio between the beginning and the tail of the pulse will be different from when only one of the scintillators has fired.

5.3.2 CsI(Tl) and BC-454 on the same PMT

Figure 5.13 shows an oscilloscope view of the pulses coming from the PMT with a BC-454 and a CsI(Tl) scintillator mounted on it. In the figure there are two channels, 1 and 3 (numbers along the left edge), which show the same signal but at different positions in time. Channel 2 in the oscilloscope shows the gate pulse fed to a QDC. It is during the length of the gate pulse that the signals to the QDC are integrated, and these integrals are what the data recorded consists of. The part in the gate from the latest pulse, channel 1, consists mainly of the fast pulse from the plastic BC-454 scintillator. The whole of this pulse lies in the gate. Looking at channel 3, the part that comes from the BC-454 scintillator comes before the gate, and the part of this signal that is integrated comes almost exclusively from the CsI(Tl) scintillator.

The small CsI(Tl) crystal is used in this case. The scintillator configuration is the one seen in Figure 5.1.

The detector set-up should be able to see 478 keV gamma photons in the CsI(Tl)

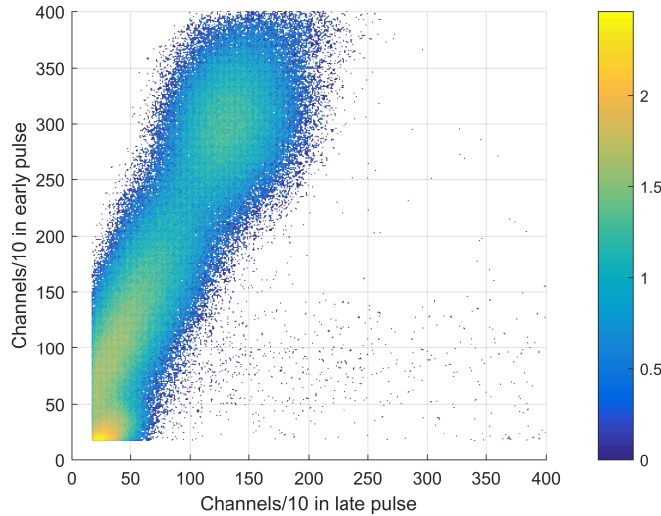


Figure 5.14: 2D energy histogram of a ^{22}Na source with the data presented in logarithmic scale. The abscissa displays the charge deposited by the late pulse in the QDC gate and the ordinate the charge from the early pulse.

crystal and the reaction products of the $^{10}\text{B} + n$ reaction in the BC-454 scintillator simultaneously. The response of the BC-454 scintillator to neutron radiation is known for some PMT gains, e.g. at a PMT bias of 2.20 kV as in Figure 5.6b, when the whole pulse lies in the QDC gate. The response in terms of channel number is about 1800 for 2.20 kV PMT bias, which is taken to be a reasonable number.

How to integrate the CsI(Tl) part of the pulse is tried out based on the scheme described in Section 5.3.1 and the fact that it should work at a PMT bias of 2.20 kV. After trials observing the peak from the 511 keV photons from a ^{22}Na source the pulse configuration shown in Figure 5.13 is chosen. A 2D energy histogram generated by a ^{22}Na source is shown in Figure 5.14. The integrated part of the late pulse, i.e. the one in oscilloscope channel 1 in Figure 5.13, is shown on the abscissa, and the integrated part of the earlier pulse, the channel 3 one in Figure 5.13, is displayed on the ordinate.

The 511 keV peak is seen at coordinates (130,300), and the peak is very broad. The difference of the response of the detector if a 478 keV photon entered it instead of a 511 keV one would not be significant considering the broadness of the 511 keV peak. A neutron event in the detector would then be a simultaneous release of scintillation light from the BC-454 scintillator giving rise to a signal at channel 1800 (180 in the 2D spectrum) in the late pulse and nothing in the early pulse, and a 1300 (130 in 2D) channel contribution from the 478 keV photon in the late pulse and a 3000 channel signal in the early pulse. This would put a registered neutron event at about the coordinates (310, 300) in a 2D energy histogram of the same type as Figure 5.14 if linearity of the system is assumed, which it can be as a good approximation.

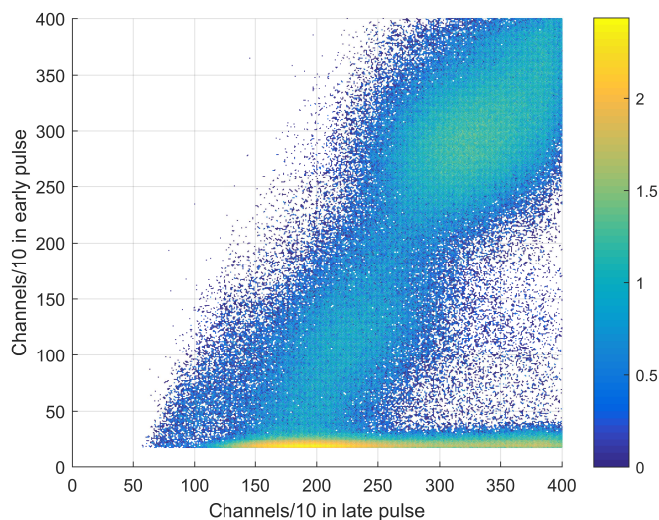


Figure 5.15: 2D energy histogram of neutron signals. Neutron radiation from a PuBe source. Logarithmic scale on the colour surface (applicate/z-axis).

A 2D energy histogram of neutrons taken by the principle described above is shown in Figure 5.15. There is a peak at channel coordinates (310,300). The events in this peak are interpreted as neutron events. The number of neutron events in that peak is 9137 per hour as measured in a region with the shape of a tilted ellipse between channels 236 and 341 on the abscissa and between channel 276 and 376 on the ordinate.

Figure 5.16 shows an energy spectrum of the late pulse which contains the whole of the BC-454 scintillator signal. The peak in this spectrum comes from the boron neutron reaction signal. The number of events in this peak, between channels 1162 and 2440, is 184678 per hour. This is about 20 times more than the number observed in the neutron peak in Figure 5.15.

To test the ability to discriminate against a background of gamma radiation, an equivalent measurement to the ones described above was conducted, but with both a PuBe and a ^{22}Na source present. The result of this is seen in Figure 5.17. The region of events originating from gamma radiation signals from the ^{22}Na (cf. Figure 5.14) is separated from the neutron signals (cf. Figure 5.15).

The number of counts per hour in the same region described as containing neutron events in Figure 5.15 is actually lower in Figure 5.17 than in 5.15, about half. This difference is ascribed in some extent to energy drifts experienced in the system, that the neutron events do not lie at exactly the same energies in this measurement as in the previous. Another contributing factor may be increased registered activity, which would decrease the live-time of the system.

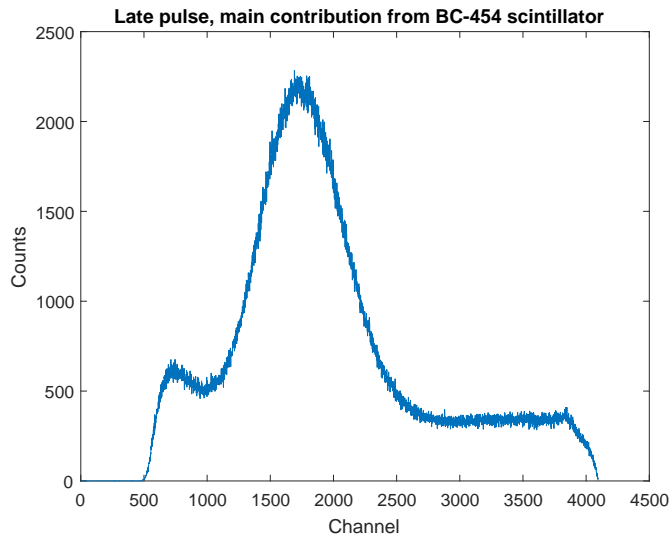


Figure 5.16: The later of the pulses in which the BC-454 signal is fully in the gate and gives a large contribution

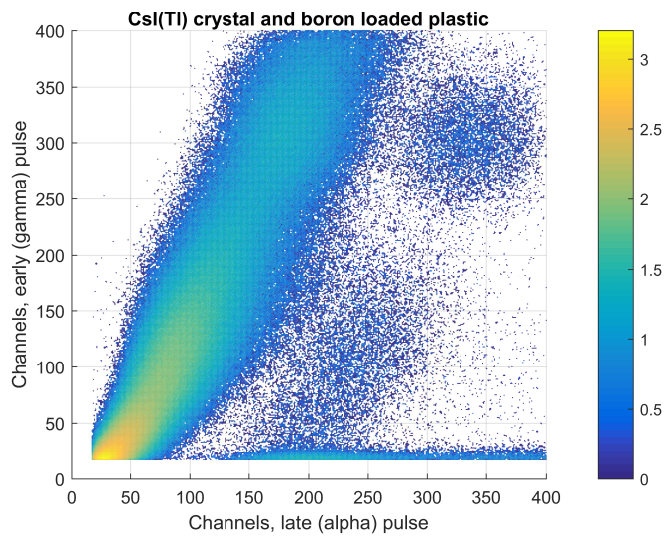


Figure 5.17: 2D energy histogram by a CsI(Tl) and a BC-454 scintillator. Both a ^{22}Na source and a PuBe source was present. Logarithmic scale on the colour surface.



Figure 5.18: The placement of the pulses from the combined signals from the P420 and BC-454 scintillators in a gate.

5.3.3 P420 and BC-454 on the same PMT

The corresponding oscilloscope view to Figure 5.13 for the CsI(Tl) case, is shown in Figure 5.18 for the case of a P420 scintillator. The P420 crystal is a bright scintillator compared to the BC-454 one, and some considerations will have to be made if an analogous set-up to the CsI(Tl) one shall be done.

The CsI(Tl) crystal is also bright compared to the BC-454, but the CsI(Tl) crystal sends out its light for a much longer duration. This can be seen if Figures 5.13 and 5.18 are compared with each other. Notice the scale difference on the oscilloscope view, seen in the top left corner of the pictures. After about 100 ns the BC-454 pulse have died out fully and only the inorganic crystal signal remains.

The shorter decay time of the P420 scintillator will have as a consequence that a larger part of the crystal scintillator pulse will overlap with the BC-454 scintillator pulse. If then the PMT bias is brought up to the region around 2.20 kV where the BC-454 scintillator produces a signal of appropriate magnitude, these signals will be drowned by the pulses from the P420 crystal.

The tail of the pulse from the P420 signal is also quite short, and not much charge is contained in that part of the pulse. This suggests that the pulse will need to be quite large for the BC-454-free part of the pulse to be of enough magnitude.

These criteria are fulfilled by attenuating the scintillation light from the P420 crystal with a filter, and also attenuating the late pulse by means of an attenuator module to make the tail of the pulse stronger in a relative sense. A mounting configuration of the scintillators on a PMT is seen in Figure 5.19.

In the figure two ND-filters (Neutral Density filters) are inserted between the two scintillators to attenuate the light from the topmost P420 crystal before it arrives at the PMT. ND-filters attenuate a rather constant fraction of the light of the whole visible spectrum. The ones used here transmitted about 25 % of the incoming light. This distorted the pulses from the P420 to much actually, so the approach was altered. Instead the area of the P420 crystal which sent out



Figure 5.19: The mounting of a BC-454 and a P420 scintillator on a PMT with a pair of ND-filters in between the scintillators.

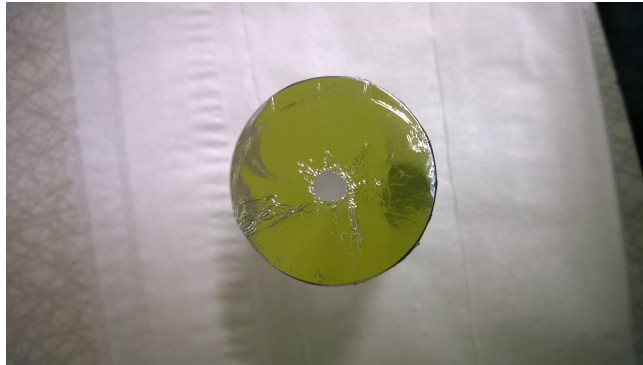


Figure 5.20: The P420 end clad in aluminium foil with a small outlet for scintillation light.

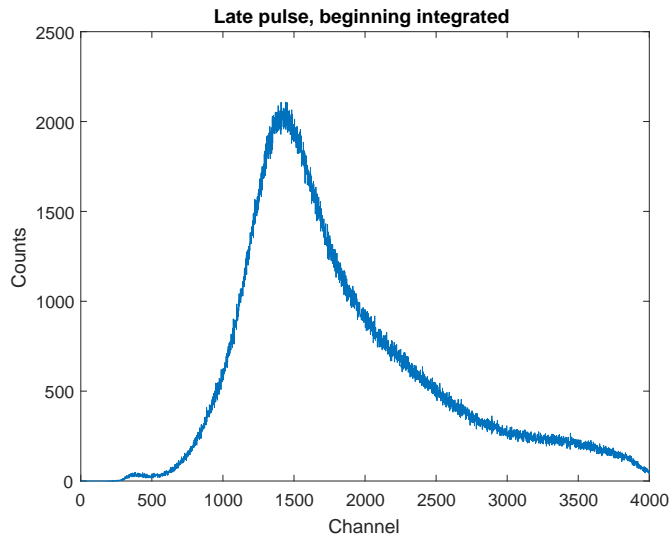
light was shrunk by applying foil of aluminium with a hole in it to let through a limited amount of light, shown in Figure 5.20.

The signal was still satisfactory out of the scintillator with the aluminium cladding, but not attenuated enough. The inside of the aluminium was therefore covered in black tape to absorb some of the signal. This, however, distorted the signals too much. Instead, the aluminium cladding without black tape was used in combination with one of the ND-filters. The output of this set-up was deemed satisfactory. This is where the pulses seen in Figure 5.18 come from, with a PMT bias of 2.30 kV and the late pulse attenuated to 0.3 times of its original size, and the size of the early pulse.

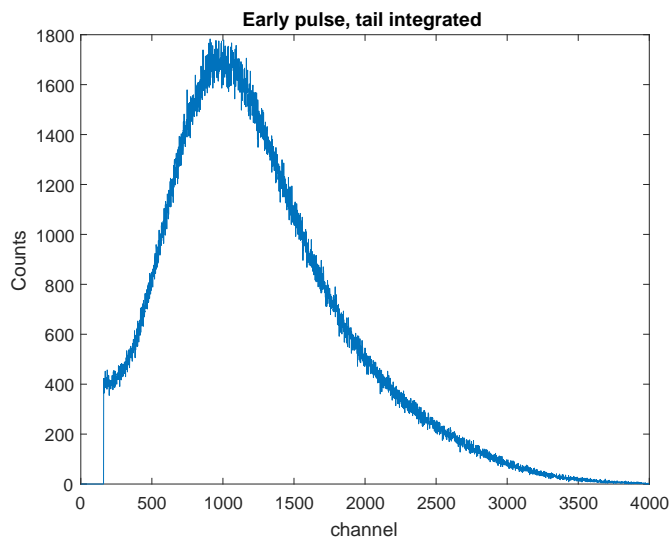
The response of this set-up to a ^{22}Na gamma source is presented in Figure 5.21, for the late pulse in Figure 5.21a and the early one in Figure 5.21b. The large peaks seen in the figures are the 511 keV photoabsorption peak riding on the signals from the intrinsic activity displayed in Figure 5.8.

The result of combining the late and early pulses into a 2D histogram with the coincident pulse energies plotted against each other is seen in Figure 5.22. If the same logic is applied here as was for the CsI(Tl) case regarding the location of the neutron signals in the 2D spectrum, the 478 keV gamma signal would be placed approximately at the same location as the 511 keV peak is placed now in an energy histogram from the early pulse. The 478 keV response from the P420 crystal in the late pulse would be added to the response from the nuclear reaction with ^{10}B and a neutron in the BC-454 plastic. The peak from these events in the BC-454 scintillator would lie at a channel number of about $1800 \cdot \frac{3}{2} \cdot 0.3 \approx 800$. This is because the result would be channel 1800 at a PMT bias of 2.20 kV, the PMT gain increases with about a factor $3/2$ when the bias is increased to 2.30 kV (extrapolated from the gain curve of the PMT [31]) and the signal is attenuated to 0.3 times its original size. Thus the neutron events would be grouped around coordinates (220,90) (or in the vicinity at least) in an analogous 2D plot to the one in Figure 5.22 but with a neutron source instead of a gamma source).

This is shown in Figure 5.23, i.e. a PuBe source is used instead of a ^{22}Na . The pulses from the intrinsic activity of the P420 crystal is fully dominating



(a) Late pulse



(b) Early pulse

Figure 5.21: The energy spectra from the late and early pulses (as seen in Figure 5.18) by a ^{22}Na source.

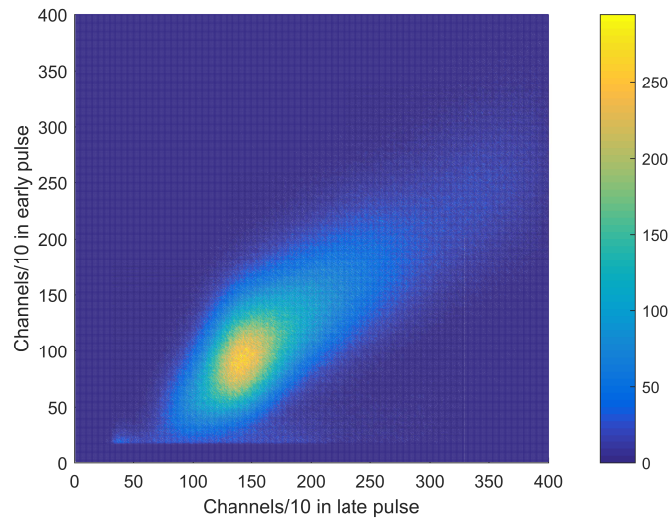


Figure 5.22: 2D histogram as created from the coincident pulses in Figure 5.21a and 5.21b.

the spectrum, making nothing else discernible. At this scale it seems that the region of interest would lay outside the internal activity in the figure. The scale is therefore changed to see areas with a lower number of counts.

Figure 5.24 shows the same thing as Figure 5.23, but with the scale of the counts cut off at 10. At this scale the region where the neutron signals are predicted to lay is covered by the intrinsic activity of the P420 scintillator.

It is then concluded that the neutron signals can not be seen by this particular configuration with this particular settings. It is however entirely possible that there may be some way to configure the scintillators and the read out system to be able to separate out the neutron signals from the gamma signals using the P420 crystal.

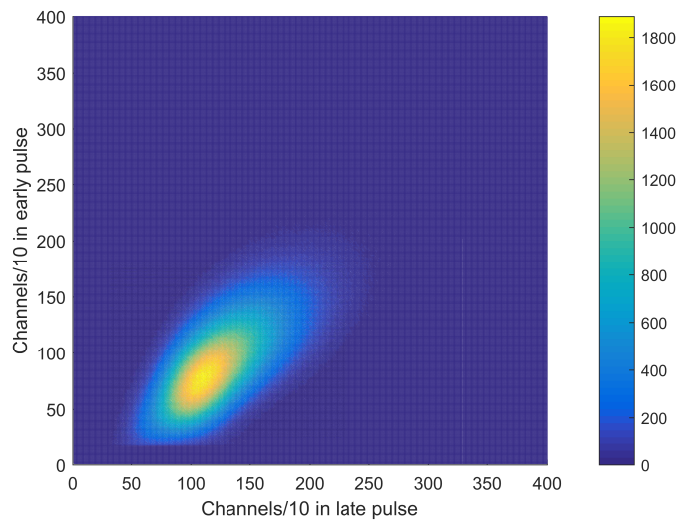


Figure 5.23: 2D energy histogram of a PuBe neutron source

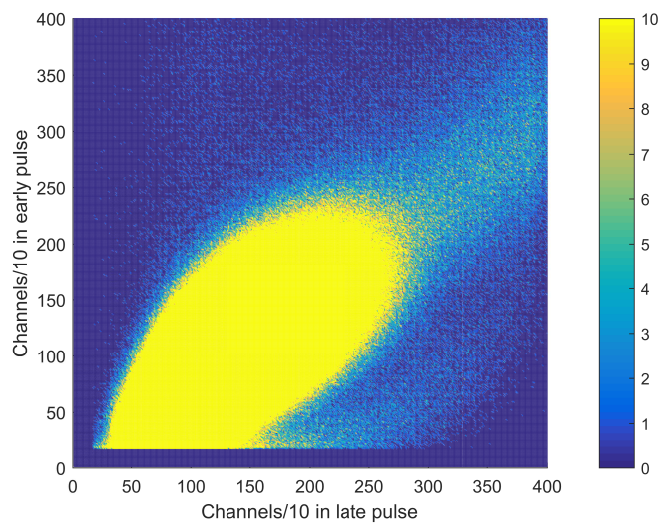


Figure 5.24: 2D energy histogram of a PuBe neutron source, with a cut off scale

Chapter 6

Boron Carbide Coated Diodes

Small Hamamatsu S1223-01N silicon PIN photodiodes has been coated with boron carbide (B_4C) at ESS Linköping. The alpha particle (or 7Li ion) released after a neutron is captured by a ${}^{10}B$ atom may then enter the depletion region of the diode and induce a signal directly.

Two boron carbide coated silicon diodes were tested, and these are shown in Figure 6.1. In the figure the boron carbide layer is seen as a gray square in the center of a blacker active silicon diode region. The whole diode area is thus not covered in boron carbide. This is because there was some concern that if the boron carbide happened to cover the electrode by the edge of the diode it would not work any more. The sides of the diode was then covered with tape, and the coating was limited to the area in the middle as seen in the figure.

The topmost one of the diodes in Figure 6.1 will henceforth be referred to as “coated diode A” and the bottom one “coated diode B”. One diode of the same type that had not been coated was also tested and will be referred to as the “blank diode”.

The measurements conducted using the coated diodes were with a ${}^{228}Th$ source and a PuBe source. The ${}^{228}Th$ measurements were done to test the diodes, whether they still worked or not after the coating process. The data from the measurements is also used to calculate the thickness of the coated layer. The PuBe source was used to determine if the coated diodes could be used to detect neutrons or not. The results from these measurements will be presented in this chapter.

6.1 Thorium spectra

The coated diodes A and B as well as the blank diode was put one at a time in a vacuum chamber with a ${}^{228}Th$ alpha particle source. The diodes were used with a reverse bias of 30 V applied via a preamplifier, which also received the signal from the diodes. A shaping amplifier was then used to shape the signal from the preamplifier, before sending the shaped unipolar pulse to an ADC. A



Figure 6.1: Two diodes coated with boron carbide

bipolar pulse from the amplifier was sent to a crossover timing SCA which then would send a signal to a gate generator to create a gate for the ADC.

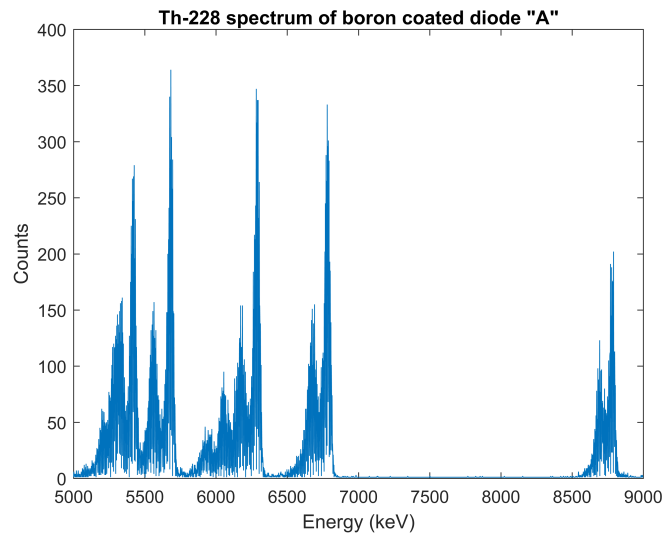
The resulting spectra are shown in Figure 6.2. The abscissae in the spectra have been cut below 5 MeV since no peaks were showing there and to make the peak structure present more visible. The energy of the peaks are known, and the figures are energy calibrated individually from the peaks present.

The energy spectra of the coated diodes shown in Figures 6.2a and 6.2b have doublet peaks, one taller and thinner a bit higher in energy and one smaller and wider a bit lower in energy. This comes from the fact that only part of the diodes' areas are covered by boron carbide. The higher narrow peak originates from the alpha particles that comes directly into the diode, while the lower one comes from the particles that has gone through the layer of boron carbide. This makes it possible to calculate the thickness of the boron carbide layer based on the difference in energy between the peaks as is done below.

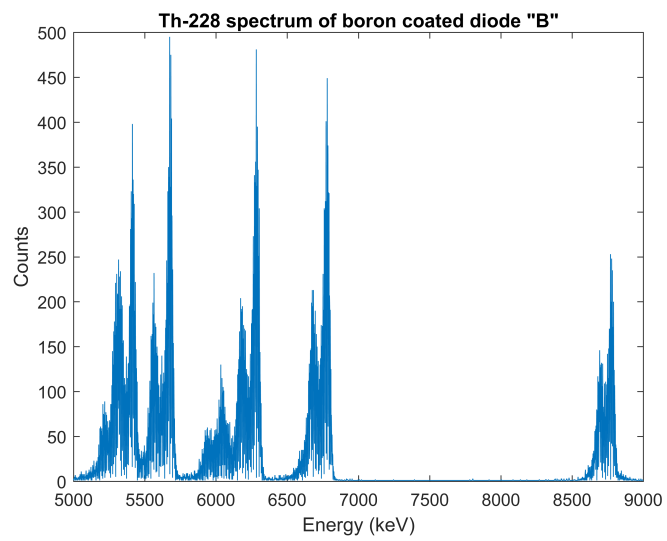
6.2 Thickness of coating layer

The stopping power of an alpha particle in boron carbide (B_4C) is calculated in SRIM for different energies as shown in Table 6.1. The energies in the table are the approximate energies of four of the peaks in the spectra in Figure 6.2. The peaks at other energies are mixed together with each other which makes them difficult to separate and are therefore excluded from these calculations. In Table 6.1 are also shown the energy difference between the peak energy of the α -particles that has missed and gone through the boron carbide layer.

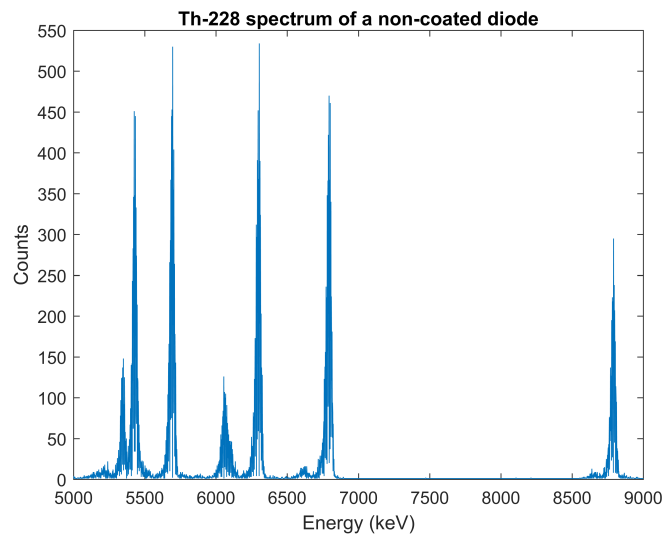
The coating thickness is then calculated as $\frac{\text{Peak energy difference}}{\text{Stopping power}}$ for each energy, and then the average of this for the four energies. The result is a thickness of $0.89 \mu\text{m}$ for the layer on diode A and $0.83 \mu\text{m}$ on diode B.



(a) Coated diode A



(b) Coated diode B



(c) Blank diode

Figure 6.2: Th-228 spectra of two boron carbide coated diodes and one non-coated diode

Table 6.1: The stopping power of an alpha particle in B_4C for four different energies

α -particle energy (keV)	Stopping power (keV/ μm)	Peak difference diode A (keV)	Peak difference diode B (keV)
5690	134.7	125	119
6290	124.8	108	103
6780	117.8	101	95
8790	970.5	89	80

6.3 Neutron measurement

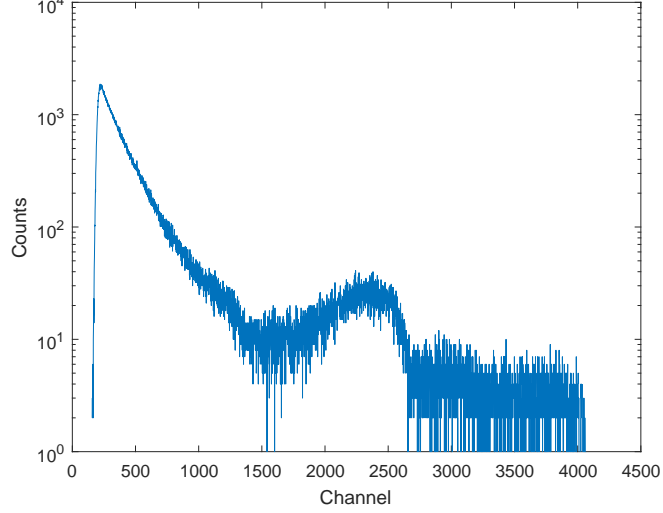
A plutonium-beryllium (PuBe) neutron source was used to test the neutron detection ability of a boron carbide coated diode. The source was enclosed in a plastic water tank for moderation of the neutrons. The coated diode A was put just outside the water tank with the PuBe material in it to test if the neutron radiation would induce a discernible signal in the diode. The blank diode was also used as a reference as to what signals don't come from reactions in the boron carbide layer. The same experimental set-up as for the thorium measurements described in Section 6.1 was used, except that the measurements were conducted in air and not vacuum, and a higher gain on the amplifier was used. The amplifier gain was increased five times, which would put an alpha particle with energy 1.47 MeV just under channel 3000.

Figure 6.3a shows the spectrum obtained by coated diode A, while the spectrum in Figure 6.3b is taken with the blank diode. The peak structure seen at around channel 2500 in Figure 6.3a is not visible in Figure 6.3b, which is pointing towards that this structure comes from the boron carbide layer and is created by the alpha particles released in the $^{10}\text{B}(n, \alpha)^7\text{Li}$ reaction. If the slope at the high end of the peak in Figure 6.3a is extrapolated towards higher energies it will end a bit below channel 3000, as was predicted. This also points towards that it is the 1.47 MeV alpha particles that creates the peak.

In Figure 6.3c the spectrum from coated diode A in Figure 6.3a has been subtracted by the one from the blank diode seen in Figure 6.3b. There the ordinate axis displays the counts per hour. This is meant to pronounce which signals originate from the boron coating and which do not. The peak from the alpha particles is clearly visible, and also some low laying noise. The noise levels do probably differ somewhat between the measurements because the measurement system is sensitive and may experience different backgrounds from occasion to occasion. Some of the low level signals in Figure 6.3c, and also in 6.3a, will come from the lithium ion entering the diodes active region, and the alpha particle signal is apparent in both Figures 6.3c and 6.3a.

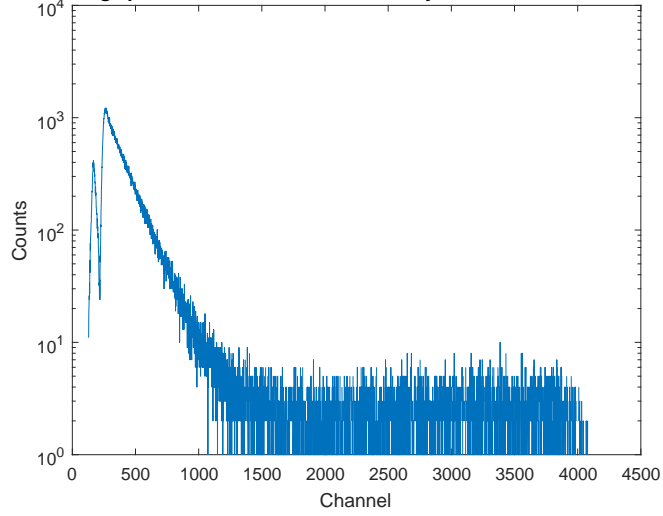
There is no lead shielding between the PuBe neutron source and the diodes in the measurement. Therefore it is a large gamma radiation background in which the measurements are conducted. The diodes are quite insensitive towards gamma radiation since the depletion region is very thin and not many photons of that high energy interacts with the Si material in such a short distance.

Lin-log spectrum of boron coated diode "A" by a PuBe neutron source



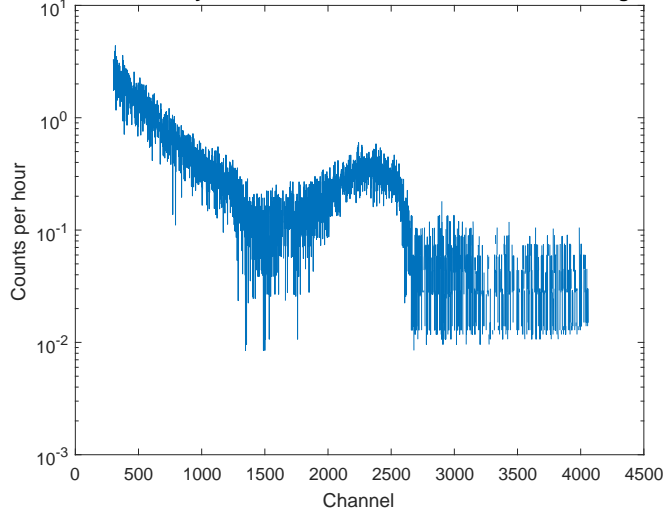
(a) Coated diode A. Log scale.

Lin-log spectrum of a non-coated diode by a PuBe neutron source



(b) Blank diode. Log scale.

Coated diode "A" by a PuBe neutron source with subtracted background



(c) Coated diode with the blank diode spectrum subtracted. Result presented in terms of counts per hour in a logarithmic scale.

Figure 6.3: PuBe spectra of boron carbide coated diode A and one non-coated diode

Chapter 7

Summary of conclusions and Outlook

The most compromising feature of the boron carbide coated scintillators seems to be its black surface, considering the findings presented in Chapter 3. A way to possibly make the coated scintillators more efficient would be to coat the scintillators first with aluminium as a scintillation light reflector, and over this a boron carbide coating to make the scintillators sensitive to neutrons.

To use APDs to gather the scintillation light has proved itself to be challenging in the case of alpha particles in plastic scintillators. There are numerous reasons for this, where quenching and emission wavelength mismatch with the APDs spectral response are a few. A way to repent for the mismatch is to use a so called wavelength shifter that absorbs light of a certain wavelength region and emits a slightly shifted wavelength. Another thing to use would be a light guide to lead the light from the whole of the scintillator surface to the active APD surface. This could improve the signal further.

The APDs used in this thesis are large with a surface area of 2 cm^2 . This means that it has a large capacitance which increases the noise level in the system. If a light guide is used it might be possible to reduce the APD area to a level where the noise is reduced and not much scintillation light has been lost, i.e. an improvement of the signal to noise ratio.

For now, reading out the scintillator signals with a PMT is sufficient, and it is what is used in Chapter 5 for the neutron detector systems. The described PSD approach to separate the signals from the different scintillators when they are mounted on the same PMT works for the CsI(Tl) case. There it is possible to discriminate between photons and neutrons up to a certain level of gamma background, so long as there is time for the CsI(Tl) crystal to relax fully before being hit by another photon. If the detector would be used in a to large gamma background, the possibility exists to shield the detector from some of the gamma radiation.

The length of the CsI(Tl) pulse in time is one cause to why it is difficult to use this scintillator in a high activity environment. The system has no time to be

restored to its ground state before the next particle arrives.

When the P420 crystal is used in combination with the BC-454 plastic, it emits too much light during the lifetime of the BC-454 pulse for this to be an effective set-up. The neutron signals are not separated from the intrinsic background of the P420 crystal when used as described in Section 5.3.3.

It would thus seem that the CsI(Tl) pulse is a bit longer than optimal and the P420 pulse a bit too short. A BGO crystal was one of the alternatives that was ordered, but did not arrive in time to be tested. The BGO has a pulse length that lies between the ones of CsI(Tl) and P420 which makes it attractive to test.

Chapter 6 presented an alternative approach to the scintillators which appears promising, using boron carbide coated diodes. It is already established that it functions in a high gamma background without any means of added protection or criteria. If the signal would remain clear in proximity to spent nuclear fuel however remains unclear. The count rate is slow however, but the number of diodes can be increased and the area of boron coating per diode as well.

Since there is interest in measuring the gamma spectrum from the spent fuel as well as the thermal neutron flux, the gamma detection system would have to be added separately if the coated diode approach would be investigated further. The gamma radiation sensitivity of the scintillator based systems is both a drawback, since the neutron signals have to be extracted out of a background, and an advantage, since the gamma spectrum is interesting in itself. The energy resolution of the gamma sensitive system would need to be improved drastically however if it should be of any interest, compared to what is seen in the figures of this thesis.

Looking to the future, there are many possibilities to investigate as is discussed above. In terms of constructing a thermal neutron detector system to use on spent nuclear fuel, the most exciting option for the moment seems to be the boron carbide coated diodes. This since they maybe able to detect neutrons in a high activity environment directly, and the system would be easily scalable. The price tag of things is something that has not been mentioned through this thesis, but this system would most likely be the cheapest one.

Bibliography

- [1] Nacka tingsrätt. Dagbok. <http://www.nackatingsratt.domstol.se/Domstolar/nackatingsratt/M1333-11/M%201333-11%20Dagboksblad%202016-04-26.pdf>, visited 2016-05-27, Utskriftsdatum 2016-04-26. Målnummer M 1333-11.
- [2] Nacka tingsrätt. Ansökan of tillstånd enligt miljöbalken. http://www.nackatingsratt.domstol.se/Domstolar/nackatingsratt/M1333-11/Aktbilaga%201/flik_01a.pdf, visited 2016-05-27, Posted 2011-03-16.
- [3] SKBF. Kärnbränslecykelns slutsteg. använt kärnbränsle - kbs-3. program för forskning och utveckling. <http://www.skb.se/publikation/8594/FoU+1984webb.pdf>, visited 2016-05-27, February 1984.
- [4] SKB. Our method of final disposal. <http://www.skb.com/future-projects/the-spent-fuel-repository/our-methodology/>, visited 2016-05-27, Last edited 2015-06-05.
- [5] IAEA - International Atomic Energy Agency. IAEA Safety Standards for protecting people and the environment. Storage of Spent Nuclear Fuel. Specific Safety Guide No. SSG-15. http://www-pub.iaea.org/MTCDD/publications/PDF/Pub1503_web.pdf, visited 2016-05-28.
- [6] Dana A. Shea and Daniel Morgan. The Helium-3 Shortage: Supply, Demand, and Options for Congress, December 2010. Congressional Research Service.
- [7] G. F. Knoll. *Radiation Detection and Measurement*. John Wiley & Sons, Inc, 4th edition, 2010.
- [8] J. A. Harvey and N. W. Hill. Scintillation detectors for neutron physics research. *Nuclear Instruments and Methods*, 162:507–529, 1979.
- [9] W. R. Leo. *Techniques for Nuclear and Particle Physics Experiments*. Springer-Verlag, 2nd edition, 1994.
- [10] Kenneth S. Krane. *Introductory nuclear physics*. John Wiley & Sons, Inc, 2nd edition, 2005.
- [11] Saint-Gobain Ceramics & Plastics, Inc. BC-400,BC-404,BC-408,BC-412,BC-416 - Premium Plastic Scintillators. <http://www.crystals.saint-gobain.com/uploadedFiles/SG-Crystals/Documents/SGC%20BC400-404-408-412-416%20Data%20Sheet%281%29.pdf>, visited: 2016-05-11.

- [12] Saint-Gobain Ceramics & Plastics, Inc. BC-440, BC-440M, BC-448, BC-448M - Premium Plastic Scintillators. <http://www.crystals.saint-gobain.com/uploadedFiles/SG-Crystals/Documents/SGC%20BC440%20BC448%20Series%20Data%20Sheet.pdf>, visited: 2016-05-11.
- [13] Saint-Gobain Ceramics & Plastics, Inc. BC-454 Natural Boron-loaded Premium Plastic Scintillator. <http://www.crystals.saint-gobain.com/uploadedFiles/SG-Crystals/Documents/SGC%20BC454%20Data%20Sheet.pdf>, visited: 2016-05-16.
- [14] Saint-Gobain Crystals. Physical properties of common inorganic scintillators. <http://www.crystals.saint-gobain.com/uploadedFiles/SG-Crystals/Documents/Physical%20Properties%20of%20Inorganic%20Scintillators.pdf>, visited 2016-01-27.
- [15] A. G. Wright. Design of photomultiplier output circuits for optimum amplitude of time response. Technical Reprint R/P065.
- [16] *INSTRUCTION MANUAL, TC 454 QUAD CF DISCRIMINATOR*. http://nuchem.iucf.indiana.edu/Instrumentation/Elec_Manual/Electronic_pdfs/TC_CFD454.pdf, visited 2016-02-19.
- [17] J. Bagi, L. Lakosi, and C. T. Nguyen. Neutron producing reactions in pube neutron sources. *Nuclear Instruments and Methods in Physics Research B*, 366:69–76, 2016. <http://dx.doi.org/10.1016/j.nimb.2015.10.004>.
- [18] Decay Data Evaluation Project, Laboratoire National Henri Becquerel. Table de Radionucléides: 137-Cs. http://www.nucleide.org/DDEP_WG/Nuclides/Cs-137_tables.pdf, visited: 2016-03-07.
- [19] Decay Data Evaluation Project, Laboratoire National Henri Becquerel. Table de Radionucléides: 60-Co. http://www.nucleide.org/DDEP_WG/Nuclides/Co-60_tables.pdf, visited: 2016-03-07.
- [20] Decay Data Evaluation Project, Laboratoire National Henri Becquerel. Table de Radionucléides: 22-Na. http://www.nucleide.org/DDEP_WG/Nuclides/Na-22_tables.pdf, visited: 2016-03-07.
- [21] Decay Data Evaluation Project, Laboratoire National Henri Becquerel. Table de Radionucléides: 228-Th. http://www.nucleide.org/DDEP_WG/Nuclides/Th-228_tables.pdf, visited: 2016-03-07.
- [22] Decay Data Evaluation Project, Laboratoire National Henri Becquerel. Table de Radionucléides: 224-Ra. http://www.nucleide.org/DDEP_WG/Nuclides/Ra-224_tables.pdf, visited: 2016-03-07.
- [23] Decay Data Evaluation Project, Laboratoire National Henri Becquerel. Table de Radionucléides: 212-Bi. http://www.nucleide.org/DDEP_WG/Nuclides/Bi-212_tables.pdf, visited: 2016-03-07.
- [24] Decay Data Evaluation Project, Laboratoire National Henri Becquerel. Table de Radionucléides: 220-Rn. http://www.nucleide.org/DDEP_WG/Nuclides/Rn-220_tables.pdf, visited: 2016-03-07.

- [25] Decay Data Evaluation Project, Laboratoire National Henri Becquerel. Table de Radionucléides: 216-Po. http://www.nucleide.org/DDEP_WG/Nuclides/Po-216_tables.pdf, visited: 2016-03-07.
- [26] Decay Data Evaluation Project, Laboratoire National Henri Becquerel. Table de Radionucléides: 212-Po. http://www.nucleide.org/DDEP_WG/Nuclides/Po-212_tables.pdf, visited: 2016-03-07.
- [27] A. Bodahl. Characteristics of B₄C Coated Scintillators. Bachelor of science thesis, Lund University, December 2015.
- [28] Carina Höglund, Jens Birch, Ken Andersen, Thierry Bigault, Jean-Claude Buffet, Jonathan Correa, Patrick van Esch, Bruno Guerard, Richard Hall-Wilton, Jens Jensen, Anton Khaplanov, Francesco Piscitelli, Christian Vetter, Wilhelmus Vollenberg, and Lars Hultman. B₄C thin films for neutron detection. *Journal of Applied Physics*, 111(10), 2012.
- [29] R³B collaboration. Technical Report for the Design, Construction and Commissioning of The CALIFA Barrel: The R³B CALorimeter for In Flight detection of γ -rays and high energy charged pArticles. Technical report, FAIR/NUSTAR/R³B/TDR CALIFA, November 2011.
- [30] Hamamatsu Photonics K.K. Si APD S8664 series - Short wavelength type APD. https://www.hamamatsu.com/resources/pdf/ssd/s8664_series_kapd1012e.pdf, visited: 2016-05-12.
- [31] Photonis. Photomultiplier XP2262. <https://my.et-enterprises.com/pdf/XP2262.pdf>, visited: 2016-05-12.
- [32] V.I. Tretyak. Semi-empirical calculation of quenching factors for ions in scintillators. *Astroparticle Physics*, 33(1):40 – 53, 2010.
- [33] William G. Lawrence, Gyula Varadi, Gerald Entine, Edward Podniesinski, and Paul K. Wallace. A Comparison of Avalanche Photodiode and Photomultiplier Tube Detectors for Flow Cytometry. In *Proceedings of SPIE - The international society for optical engineering*, March 2008.
- [34] Saint-Gobain Ceramics & Plastics, Inc. PreLude 420 data sheet. <http://www.crystals.saint-gobain.com/uploadedFiles/SG-Crystals/Documents/PreLude%20420%20data%20sheet.pdf>, visited: 2016-04-27.